RADIOTRONICS

IN THIS ISSUE

We are pleased to present this month
another AWV contribution to the
1963 I.R.E.E. National Convention.
This paper has many aspects of great
interest, and is a good example of
the investigatory work which is
carried on continuously in the search
for the highest attainable quality in
the product.

This is the first of a series of articles
dealing with all aspects of photo-
tubes and photocells. With the
growth of industrial electronics,
these devices, and others, are diver-
sifying into almost every type of
industry and activity.

5

An Investigation of a Television Picture Tube Gun

by D. M. SUTHERLAND, B.Sc.

Amalgamated Wireless Valve Co. Pty. Ltd.

Electron path tracing equipment based on the electrolytic tank analogue of the electrostatic field has been used to trace electron paths through an electron gun of a design commonly used in modern television picture tubes. A description is given of the gun models and the technique of using the equipment. Models were made of three parts of the gun: the cathode system, the accelerating system and the final electrostatic focusing lens; and electron paths were traced in each of these sections of the gun under various conditions. The growth of screen spot size with "drive" is discussed; previously published results on spherical aberration in electrostatic lenses are used in support to explain this feature of the gun. The use of the gun as a crude electron microscope in examining its own cathode during manufacture is also explained.

Introduction

The investigation reported here was carried out with the object of acquiring greater familiarity with the basic operation of the picture tube gun; for the purposes of assisting the most rapid solution of certain production problems; of enabling the best choice to be made from available design variations; and of contributing to the understanding of the operation of the picture tube in a television receiver.

The experimental equipment used in this investigation has been described by Hollway[1].

Many of the problems of picture tube gun design have been discussed by a number of authors, for example: Law[2], Maloff and Epstein[3], Allard[4], Francken, de Gier, and Nienhuis[5], Knechtli and Beam[6], Pearce[7], Burdick[8], Tsukkerman[9]. What was sought in the present investigation was information on the particular design which (with variations between manufacturers) is quite the most widely used in commercial picture tubes of all makes.

The important dimensions of three such variations are shown for record in Fig. 1. The particular gun studied was (C), known as type 8235 in our factory.

All these guns have the same basic electrode arrangement. They are designed for electrostatic focus, electromagnetic deflection (with an external yoke) and have no ion trap. The electrodes are drawn from stainless steel sheet (with the exception of the nickel cathode); all have cylindrical symmetry, and are assembled as accurately as possible on a common axis.

1. Hollway, D. L., "An electrolytic tank equipment for the determination of electron trajectories, potential and gradient", *Proc. Inst. E.E.*, **103 B**, No. 8, 1956.
2. Law, R. R., "High current electron gun for projection kinescopes", *Proc. Inst. Rad. Engrs.*, **25,** 1937, 954.
3. Maloff and Epstein, "Electron Optics in Television", 1938, McGraw-Hill.
4. Allard, L. S., "Design factors in television cathode ray tubes", *Proc. Inst. E.E.*, IIIA, 1952, 499.
5. Francken, J., de Gier, J., and Nienhuis, W. F., "A pentode gun for television picture tubes", *Philips Tech. Rev.*, 1956, **18,** No. 3, 73.
6. Knechtli, R. and Beam, W. R., "Kinescope electron guns for producing non circular spots", Industry Service Laboratory Report RB60, R.C.A., July 1956.
7. Pearce, R. R., "The return of electrostatic focussing", *Journ. of the Television Soc.*, **8,** 1957, 237.
8. Burdick, G. A., "A new approach to short picture tube design", *The Sylvania Technologist*, **12,** No. 1, 1959, 2.
9. Tsukkerman, I. I., "Electron Optics in Television", Pergamon, 1961. Trans. from the Russian.

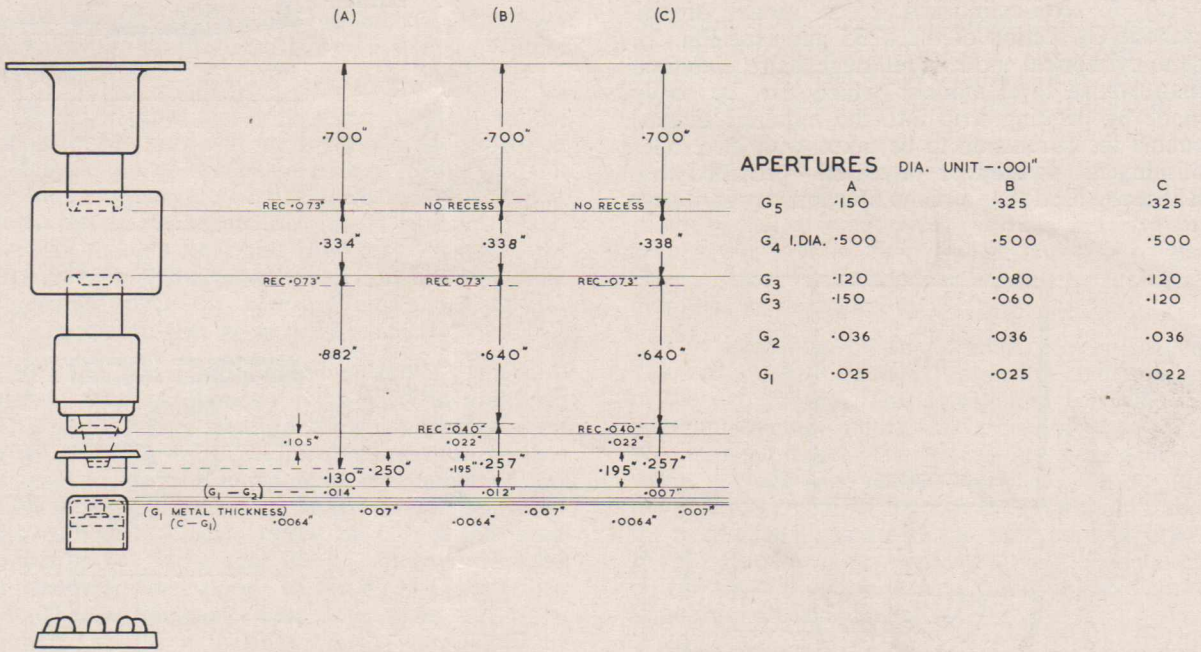| APERTURES DIA. UNIT – .001"		
	A	B	C
G_5	.150	.325	.325
G_4 I.DIA.	.500	.500	.500
G_3	.120	.080	.120
G_3	.150	.060	.120
G_2	.036	.036	.036
G_1	.025	.025	.022

Fig. 1—Dimensions of three CRT guns.

Fig. 2 has been drawn to illustrate the structure of this type of gun and the way it produces a narrow beam of electrons. For clarity the scale has been considerably distorted. The general electron optics of this kind of gun are well described in the literature[10 et al.].

The electrodes in order are: cathode (with internal heater), modulating electrode G_1 screen G_2, accelerating electrode G_3, focus electrode G_4, and final anode G_5. Typical operating voltages are shown in Fig. 2.

Electrons from the cathode are focussed to a "cross-over" by the cathode-G_1-G_2 system. The beam thus formed is accelerated between G_2 and the first G_3 aperture, and some focussing also takes place in the lens system between G_2 and G_3. The space between the G_3 apertures is of nearly uniform potential and serves only as a drift space, the final focusing of the beam being carried out by lens formed between G_3 (second aperture) G_4 and G_5. After leaving G_5 the beam travels through a region of uniform electrostatic potential to the screen, being deflected by the magnetic field applied by the external deflection yoke.

The normal operating voltages have been quoted; however there is another set of voltages used during manufacture in the factory—viz. that for the "cathode test" condition. These voltages are typically: cathode-zero; G_1 varied upward from cut-off (at say — 60); G_2 + 400; G_3 + 4000; G_4 — 600; G_5 + 4000. When "cathode

test" voltages are applied and properly adjusted (no deflection is used), an enlarged image appears on the fluorescent screen of the tube which to all intents and purposes gives an electron picture of the important emitting area of the cathode and enables its emitting quality to be judged.

Models

The working dimension of the tank in the equipment used[1] are approximately 44 in x 22 in x 11 in. Another relevant dimension is the distance between the two potential gradient probes (approx. 0.10 in). With these sizes in mind, scale factors of 25 x and 150 x were chosen, and the following models constructed.
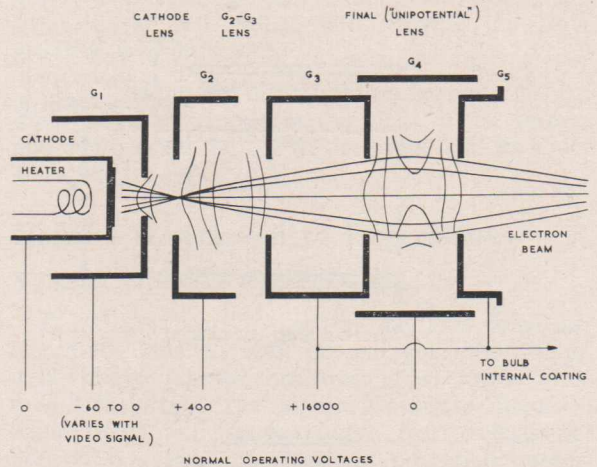

Fig. 2—Picture tube gun schematic.

10. Zworykin, V. K., and Morton, G. A., "Television", Wiley 1954, 2nd Ed.

(a) A semi-cylindrical 25 x model of the cathode-G_3 section of the 8235 gun (see Fig. 3). Semi-cylindrical models, although more elaborate than wedge type models (which can be easily made by bending strip into the required shapes) enable measurements to be taken with electrodes misaligned—twisted or displaced—provided that it is recognised that a plane of symmetry is always
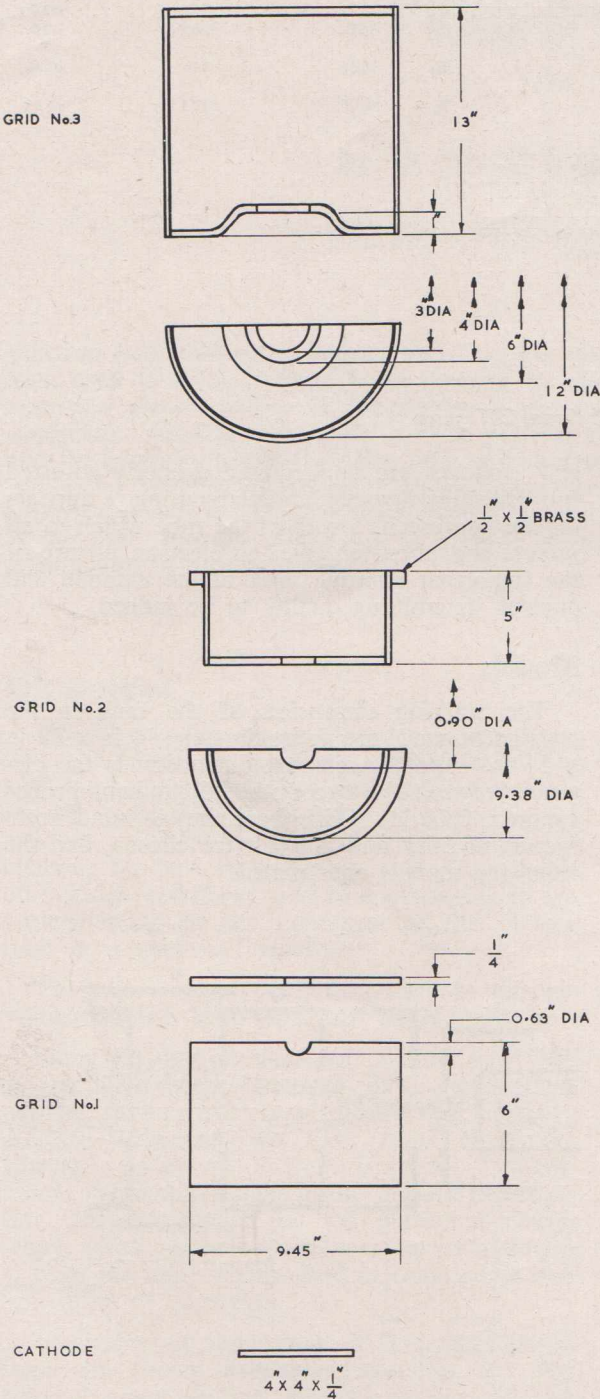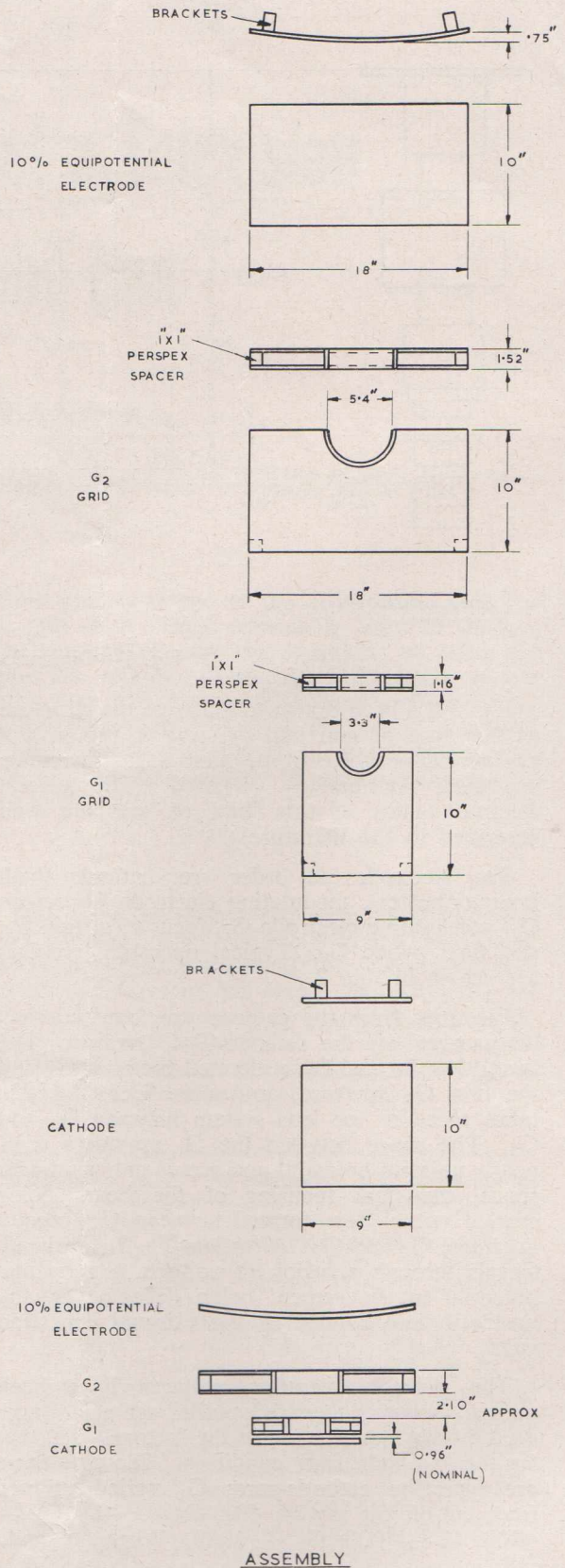

Fig 3—25-times scale model.

Fig. 4—150-times scale models, cathode G_1-G_2-section.

given by the surface of the electrolyte. They were chosen on this occasion with a view to future work.

A 25 x scale factor is about as great as the depth of the tank will allow for a model in which a fair length of the beam path is being studied. A minor advantage of this scale factor is that it turns .01 in thick material into $\frac{1}{4}$ in thick plate. It was thought that the thickness of the sheet from which the apertures are punched could be significant near the aperture edges. (Note: no conclusion on this point was reached.)

(b) The above scale factor gives a G_1 aperture size of 0.63 in diameter for a .025 in aperture. This seems rather small to allow ray-tracing using a 0.1 in probe width within this aperture; so that it was decided to make a larger model of the cathode-G_1-G_2 system to study matters close to the cathode. A scale factor of 150 x was used (see Fig. 4). Note that the G_1 aperture of 3.30 in diameter corresponds to the 8235 G_1 aperture of .022 in diameter. This large scale factor required the use of a plate which was placed to correspond to an equipotential surface (e.g. the "10% equipotential") whose position was taken from the measurements with model (a).

(c) Finally a wedge model was made, with a scale of 25 x of the final focussing system G_3-G_4-G_5. The electrodes were simply bent up from $\frac{1}{8}$ in x 2 in copper bar to match the appropriate sections. They are not illustrated as their shape is clear from subsequent diagrams (Figs. 12 and 13). This model gave information on the operation of the anode end of the gun.

Experimental Details

(a) The models are washed in chromic-sulphuric acid solution to remove surface layers (oxidation, dirt) which can cause quadrature components in the current.

(b) The models are set up in the tank and correctly aligned, the engraved lines on the baseboard in the tank being used as reference; and the tank is filled with water.

(c) The double probe is set up to rotate about the potential probe, the position of the pen then corresponding to that of the potential probe in the water. The model is then plotted out on the drawing sheet. The voltages on each electrode are set to correct value using suitable voltage taps and adjusting with the fine control potentiometer.

(d) The equipotentials in the model can now be plotted. The potentiometer R_1 (loc. cit. Fig. 2) is adjusted to the desired equipotential and the probe moved till a null is indicated. For tracing families of equipotentials a quicker method is provided by the phase sensitive detector and the electromagnetic pen. When the in-phase component of the input signal falls below a certain minimum value, an electromagnetically operated pen is brought into contact with the paper. The pen is moved backwards and forwards over the approximate position and the line is painted in as a succession of dots.

(e) Electron trajectory tracing is effected in the following manner. The test cell (parallel plates 5 inches apart were used) is next set up with 100% voltage on one plate and 0% on the other. This is used to calibrate the gradient amplifier as described by Hollway[1] (p. 159).

The mounting of the double probe is then adjusted so that it rotates about the centre point of the two probes. This is essential for accurate electron tracing if the curvature of the equipotentials is large. The probes are next aligned with the front edge of the "tricycle". To do this the electron tracer is fitted to the pantograph and the front edge aligned with the 50% equipotential. If zero gradient is not indicated the selsyn motor on the tricycle end is loosened and adjusted until zero gradient is indicated.

The tricycle is now ready for tracing and is aligned to an arbitrary starting point of an electron using the pen and wheel D (Hollway[1], Fig. 8). The path is drawn by the pen F and the radius of curvature of the path is determined by the direction of the wheel D, which may be steered about a vertical axis. The path is drawn by following the null as indicated on the CRO.

The normal hazards of experimental work were encountered, and results now and then were upset by such things as loose leads, reversed leads, and so on. It was usual to check plots and traces repeatedly and to clear up apparent inconsistencies, lack of symmetry, and the like, before proceeding.

An additional check which was found worth while was to ensure that leakage between the probes did not exist, by setting the cell to zero gradient for both negative and positive voltages on the test cell plates, and proving the zero gradient was indicated.

Such leakage did occur when a scarcely discernible crack developed in the glass of the probe; and again when the top of the probe and its leads were wet.

General Description of Experiments

Voltages expressed as percentages

It will be observed that the diagrams show the electrodes labelled with percentages rather than with voltages (shown sometimes in brackets). This follows the actual experimental procedure. Electrostatic fields and space charge free trajectories depend on ratios of electrode potentials rather than absolute values, and in fact the same voltage (the maximum available) is applied to the G_3

model for both "normal" and "cathode test" conditions, the voltages on the other electrodes being adjusted to give correct ratios as in the table below.

	Cathode		G_1		G_2		$G_3 + G_5$		G_4	
	Volts	%	Volts	%	Volts	%	Volts	%	Volts	%
Cathode Test	0	0	−20	.5	400	10	4000	100	−600	−15
Normal	0	0	−20	.125	400	2.5	16000	100	0	0

In the experiments with the 150 x model described later, it will be noticed that the potentials of G_2 and G_1 are expressed as percentages of the 100% potential which is applied to a "10% equipotential electrode"—the latter 10% referring to the potential determined in a previous experiment in which the position of this 10% equipotential was found. This procedure was necessary to limit the size of the electrode group in the large scale (x 150) experiments.

Order of experiments

It will be seen from the descriptions given above of the guns and models that the gun is divided into three sections which are investigated independently. These sections are:

    (i) the cathode-G_1-G_2 system,
    (ii) the lens set up between G_2 and G_3, and
    (iii) the final focusing lens set up by the G_3-G_4-G_5 system.

The experiments were carried out in the order shown below:

The G_2-G_3 system model was set up, and equipotentials drawn; and the required ray tracing carried out, both for "normal" and "cathode test" voltages (Figs. 5 and 6).

The larger scale cathode-G_1-G_2 models were then set up, the 100% electrode being a sheet electrode placed and shaped to give a boundary corresponding to a suitable equipotential surface as determined from the G_2-G_3 models. (The 10% equipotential from these models was generally used).

Finally, the wedge model of the G_3-G_4-G_5 system was used. For these experiments the base board in the tank was adjusted to give a 15° wedge of water, and the electrodes were placed so that the edge of this wedge corresponded to the axis of the system (see Figs. 12 and 13).

Discussion of Results
25 x G_2-G_3 models

Fig. 5 shows a typical plot taken with the type 8235 gun model. An axial path and two outer paths have been traced. The latter do not corre-
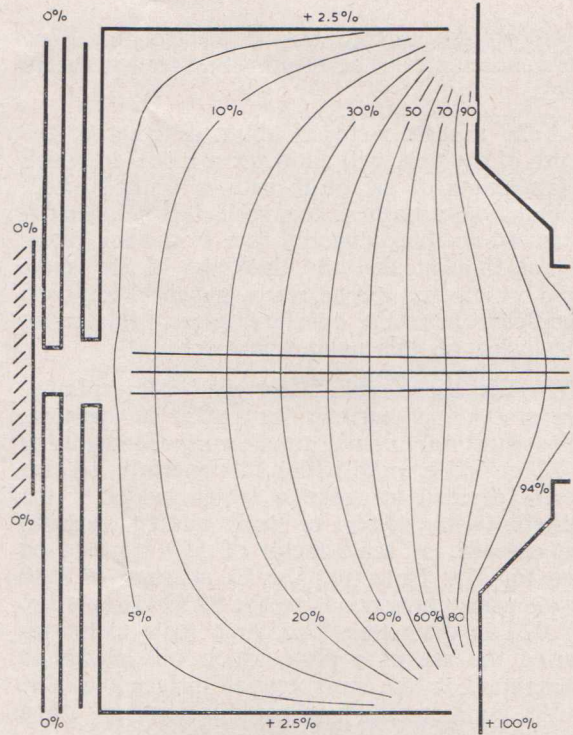

Fig. 5—Equipotentials in G_2-G_3 space, normal voltages.

spond to paths actually occuring in practice (which all originate from a "cross-over" on the axis between G_1 and G_2—as is seen below), but were put wide out because some early difficulty was experienced in starting traces very near the axis. The paths are also started away from G_2, because paths in the apertures were to be studied in the larger models.

It is clear that the main function of this part of the lens is to provide an accelerating space. There is some converging action in addition to that close to G_2 (where the curvature of the 5% equipotential is significant) and this is taken into account when the gun as a whole is being considered. In tracing actual paths through the gun we have used paths determined in later experiments as "starts" and we have thought it better to use (for such "paraxial paths very close to the axis") a numerical method of tracing paths through this part of the gun, based on the equipotential plot.

These plots are discussed later.

Fig. 6 gives the equipotential plot for the 25 x model of the 8235 gun under cathode test voltage conditions. The differences in the field in this case are clear from inspection of the figure.

150 x models of cathode-G_1-G_2 system

Fig. 7 shows the plot of equipotentials and electron paths traced using the large scale semi-cylindrical model of the cathode G_1-G_2 system
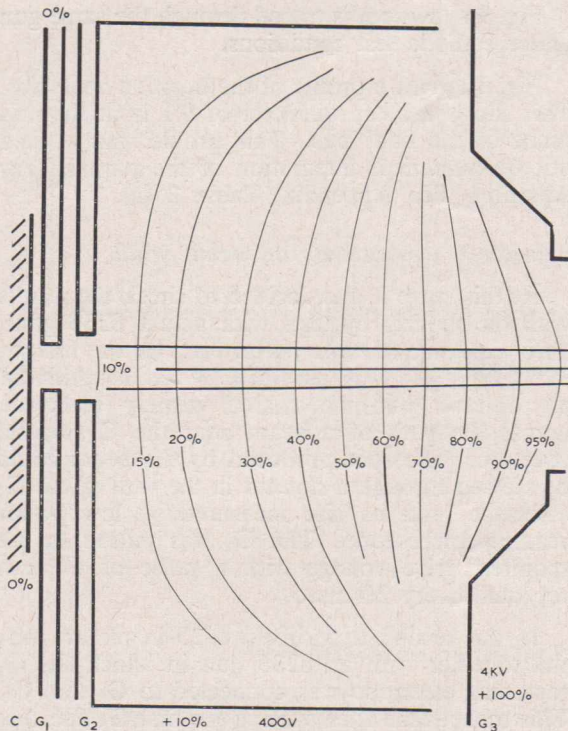
Fig. 6—Equipotentials in G_2-G_3 space, cathode test voltages.

of the 8235 gun. For reference the original diameter of the G_1 aperture is .022 in and that of the G_2 aperture is .036.

The voltages for Fig. 7 are those for normal operation with a grid bias (—32 volts) approximately mid way between cut off and zero bias, corresponding to a beam current of about 200 μa and a fairly bright patch on the screen.

The electron paths were traced in order going outwards from the axis, the outermost paths being those for which a definite "start" could be obtained. The position of the zero equipotential in this diagram explains this point further. No attempt was made to display current densities which would vary across the beam from a maximum in the centre; and further random transverse velocities introduced thermally or by roughness in the cathode surface would in practice make the edge of the beam diffuse, so that the delineation of the beam must be treated with some reserve. Space charge effects are also ignored here. It is however relevant to point out that a first-order treatment of space charge and initial thermal velocity effects does not indicate marked uncertainties. Thus if we use the "Design Chart for Calculating Beam Parameters"[11] and treat the beam as one of uniform density, we have (referring to Fig. 8 and using Hollway's symbols),

11. Hollway, D. L., "Electronics", Feb. 16, 1962, McGraw-Hill.

initial radius of beam = .0025 in ($V_i = V_c$), distance cathode to cross-over = .0125 in (Z_s).

Thus $Z_s/V_i = 5.0$.

Voltage (cathode to cross-over) = 80 (V), and

current in beam assumed to be 200 μa (I).

From the chart (loc. cit.) we find that space charge is negligible, and that the ratio "spot radius to cathode radius" is approx. 0.2—that is, thermal velocity effects would allow a spot radius of .0005 in. This corresponds at the cross-over in Fig. 7 to .15 in which is of about the same order as the cross-over size indicated in Fig. 7. This figure can be taken as an indication of the "diffuseness" of the paths at this point. A similar use of the chart indicates that this "diffuseness" could not exceed .17 in. on the scale of Fig. 7, at the 100% mark (the original 10% equipotential) where the width of the beam is .75 in. It is certainly not large enough to upset the value of our diagrams in explaining matters within the gun.

Some features of Fig. 7 will now be considered. The formation of the cross-over is clearly shown —in this case it is fortuitously sharp, or free from aberrations, to judge from succeeding diagrams. The converging action of that part of the G_2-G_3 field close to G_2 is also apparent.

Attention is now drawn to the small area of cathode which is actually emitting under conditions of Fig. 7. This is .005 inches in diameter. At greater grid bias (and smaller beam currents) it is smaller in diameter still, and it is thus clear that flaws in the cathode must be kept very small indeed if they are not to interfere with the uniformity of the beam. It can be pointed out here that the "diffuses" of the electron paths
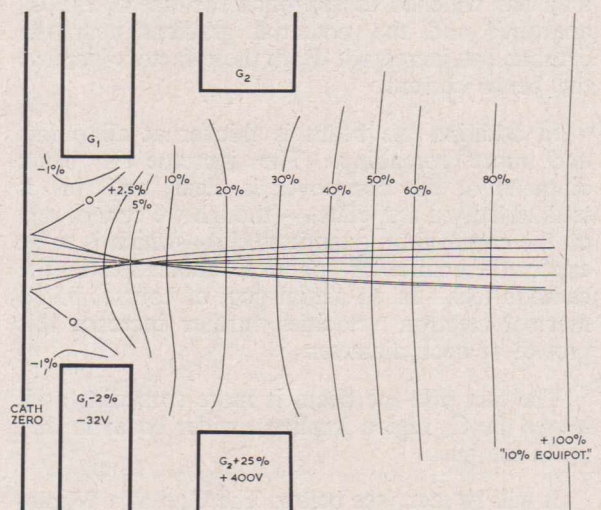

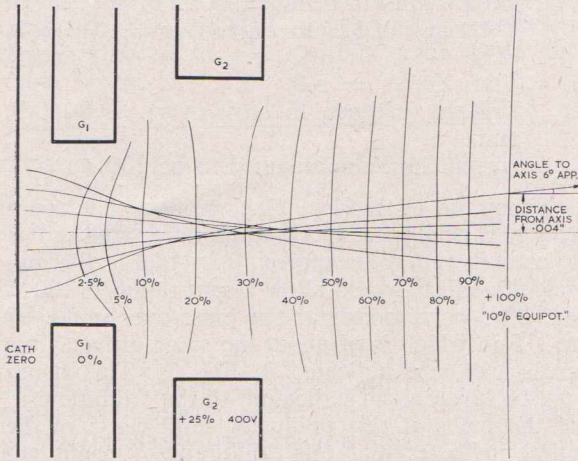Fig. 7—Equipotentials and electron paths in cathode G_1-G_2 space, normal voltages.

Fig. 8—Equipotentials and electron paths in cathode G₁-G₂ space, normal voltages, zero G₁ bias.

caused by thermal initial velocities softens but does not destroy the one to one correspondence across the beam with points across the cathode spot.

As to cathode loading, we do not know the distribution of current density across the cathode, but the average is (for a beam current of 200 μa) about 2 amp/cm². A "triangular" distribution would give twice this at the centre. Such current densities do not appear to worry the cathode as remarkably long lives are being attained by pictures tubes.

Referring now to Fig. 8 we have here a diagram of equipotentials and electron paths for the same gun, but with zero bias. The cathode emitting area has widened to approach the size of the G_1 aperture; and the potential gradient near the cathode has increased. Both these factors increase the beam current.

In addition the beam is thicker at all points and more spreading. The increase in beam diameter at the cross-over is clear, and this is undoubtedly a real effect—(though we cannot rely on the comparison quantitatively)—which is to be expected because of spherical aberration in the cathode lens. In an actual gun, of course, initial thermal electron velocities further increase this growth of neck diameter.

The fact that the beam is more spreading as it leaves the G_2 region implies a wider beam further on in the gun.

It will be seen (see below, The Gun as a Whole) that both these factors contribute to the growth of the screen spot size with beam current, inevitable in a gun using apertures.

Fig. 9 shows paths traced through the same gun under cathode test conditions.

Fig. 10 gives a profile of the beam at zero bias. This shows a beam diameter of 0.1 in at the mid plane of the final lens. This profile was worked out by numerical integration of the paraxial ray equation. See Appendix, Table 2 (a).

Subsidiary experiments on beam width

At this stage it was decided to check the results with the models by tests with actual 8235 guns. Two experiments were performed. In the first an 8235 type gun was modified by the insertion of an oblique phosphor-coated display electrode across the path of a beam near the G_3 second aperture. The spot produced by the beam could be viewed through a slot cut in the wall of the G_4 electrode; and its size measured by low power reading microscope. The G_1 was pulsed to the required drive voltage with a pulse of 6 μsec. repeated every 20 msec.

In the second experiment a 23-in picture was put together with an 8235 gun in which the G_4 focussing electrode was connected to G_3 and G_5. This meant that after passing the first G_3 aperture the beam travelled to the screen through a region of constant potential. Rectilinear paths can thus be assumed in this space and by observing the size of the spot on the screen a calculation of the beam thickness in the gun can be made. Within the limits of error in this kind of measurement we can take the beam as starting from a point at the centre of the cathode. The cathode to screen distance is about 12.5 inches. Other germane dimensions are:—cathode to G_3 aperture .84 inches; cathode to centre of G_4 1.10 inches.

Results for both experiments are shown in Fig. 11 and the agreement between the curves for the two guns is considered reasonable. Variations in the drive curves of the amout shown is normal experience.
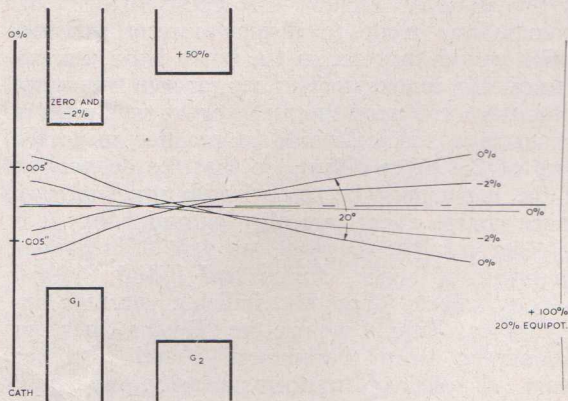

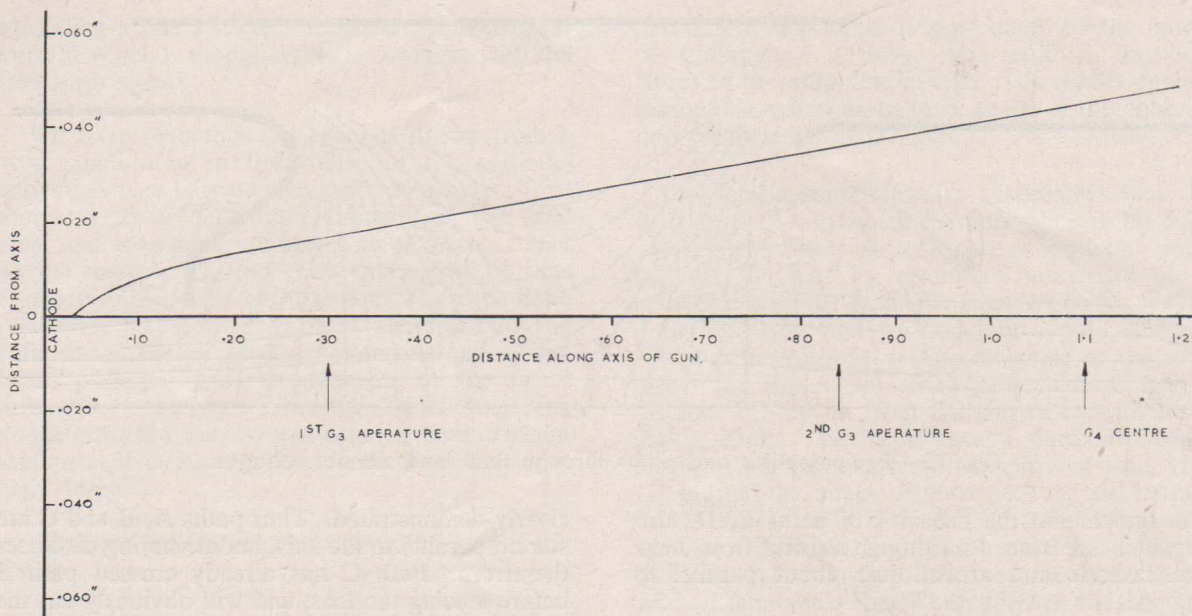Fig. 9—Electron paths in cathode G₁-G₂ space, cathode test voltages.

Fig. 10—Beam profile in 8235 gun, normal voltages, zero G_1.

Comparison of Fig. 10 and Fig. 11 shows that the trace underestimates the beam diameter quite appreciably. The reasons for the differences have not been investigated; but undoubtedly one of the reasons is the difficulty of deciding just where the outer boundary of the cathode emitting spot really lies. It is felt that the tank experiments have served their purpose in pointing out the large variation in beam diameters during drive and the large diameter of the beam at high drive voltages.

25 x "wedge" models of the final lens

Fig. 12 shows a plot of equipotentials and some electron paths for the final electrostatic lens, under normal voltage conditions.

This is a so-called "uni-potential" lens—which refers to the fact that the electrons enter and leave the lens at the same potential. In their passage through the saddle-like field of the lens, the electrons suffer in order a divergence, a convergence, and a divergence—a net convergence being produced as is indicated by all the 5 paths traced.

Paths A and B enter the lens parallel to the axis. They do not correspond to actual paths, but were traced in order to show up the spherical aberration which is well known to be produced by such a lens. Path A if produced would cut the axis approximately 27 in from the centre of the lens; and path B about 24 in (on the scale of the model).

These measurements have not very great accuracy as is obvious from the very small declination to the axis of the emerging paths. (It is

interesting to note that on the scale of the model the picture tube screen is 25 ft. distant.) We could scarcely use such measurements for example to investigate spherical aberration quantitatively— this is asking too much of the mechanical accuracy of the tracing equipment. However, we can say that paths A and B indicate a focal length of about 1.0 in. Since the cathode is at about the same distance from the final lens, we
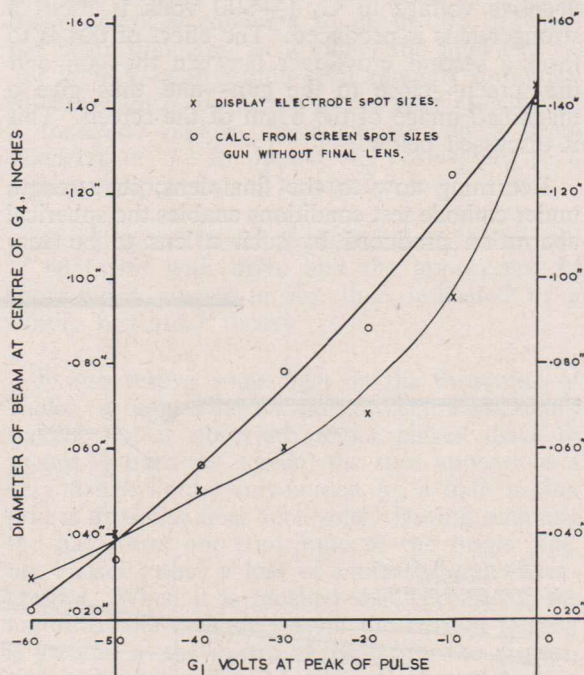

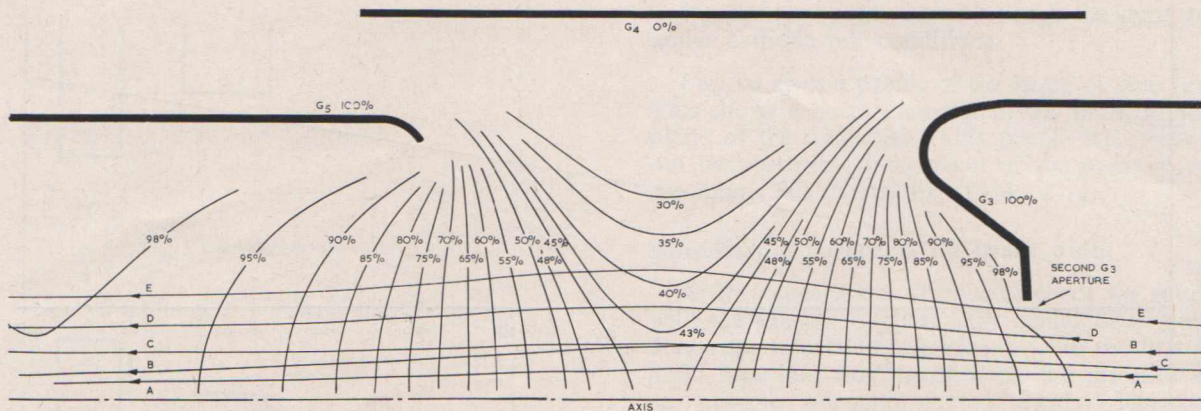Fig. 11—Measurements of beam diameter, normal voltages.

Fig. 12—Equipotentials and paths through final lens, normal voltages.

can understand the behavior of paths C, D, and E which are traced as though arising from near the cathode and are all just about parallel to the axis on leaving the lens.

In this lens the ratio of applied voltages is very high (in fact infinite when the voltage of G_4 is zero) and the action of the lens depending as it does on voltage ratios is therefore independent of variations in EHT voltage. It is also insensitive to changes in G_4 voltages of the order of 100 volts, or less. The lens is also operated under another set of voltages; the "cathode test" condition, and Fig. 13 shows paths traced through the same lens under "cathode test" conditions. For this test the voltage applied to G_3 and G_5 is lowered so that by the application of a reasonable **negative** voltage to G_4 (—600 volts is used) a stronger lens is produced. The effect of this is to form a second cross-over between the gun and the screen—close to the gun—and thus give a magnified image of the beam of the screen. This is discussed below.

Returning now to the final lens; its strength under cathode test conditions enables the spherical aberration produced by such a lens to be very

clearly demonstrated. Thus paths A, B and C are started parallel to the axis, but at varying distances therefrom. Path C has already crossed path B before leaving the lens, and will obviously cut the axis very much nearer the lens than will path B. Path B bears the same relationship to path A.

The effects of the spherical aberration in the gun were recognised early. See for example Maloff and Epstein[3]. Liebmann[12] carried out a thorough experimental investigation of a number of lenses of the type used in the present gun, and his results have been applied in the next section to explain the importance of spherical aberration in the formation of the spot on the fluorescent screen.

The Gun as a Whole: Formation of the Spot on the Screen

We can now take the gun as a whole and consider how it performs its principal tasks of

12. Liebmann, G., "Measured properties of strong equipotential lenses", *Proc. Phys. Soc. Lond.*, **62B**, 1949, 213.
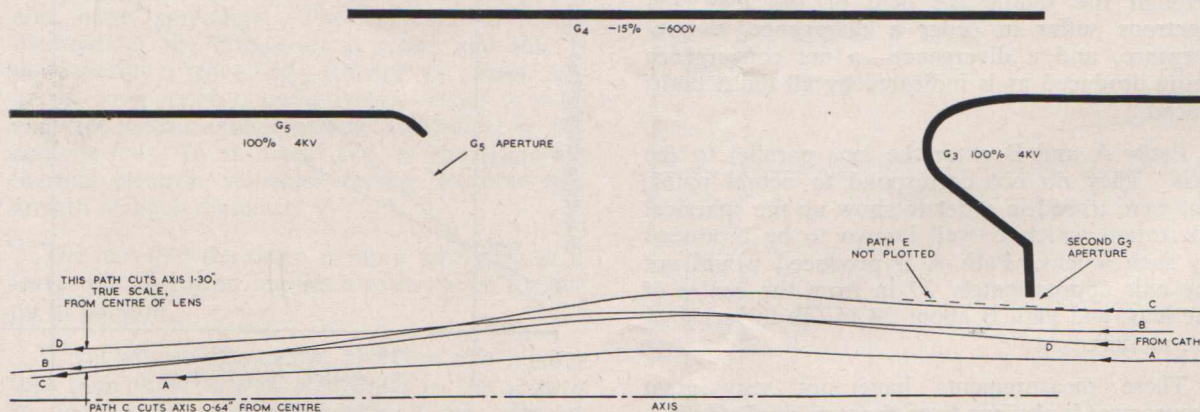
Fig. 13—Paths through final lens, cathode test voltages.

providing a fine spot on the screen, with a beam current which is modulated in accordance with the television signal.

We have seen that the beam is drawn from a very small area in the centre of the cathode, converges to a narrow neck on "cross-over", then increases to its maximum diameter in the final lens, and thereafter converges to produce a spot on the screen. We also know that as the G_1 bias approaches zero, the emitting area of the cathode increases, the voltage gradient presented to the cathode increases (both factors increasing the beam current); and the diameter of the beam throughout the gun increases—including the diameter at the cross-over—and we have a beam thickness of at least .100 in in the final lens with high "drive".

What are the factors controlling the size of the spot?

In the first place we should examine the notion that the spot on the screen should be regarded as the image of the cross-over or at least a narrow part of the beam near the cross-over, such image being formed by the final lens in the idealised manner of Fig. 14. Referring now to Fig. 8, we have an apparent cross-over diameter of approximately .001 in (true scale), produced by aberration. Applying the Hollway chart we find that initial thermal velocities require a diameter of about the same order, so that we will assume an object size of .002 in under the zero bias condition. This object is about 1.1 in from the centre of the final lens (which we will consider as a thin lens without affecting the accuracy of this particular calculation), and as we saw in the foregoing section, this lens has an apparent focal length of 1.0 in. The .002 in object is therefore in the right situation to be projected as an image on to the screen some 12 in from the lens. We would expect in this case a 12 times magnification and a spot size of .024 in.

However, a typical set of spot size measurements on a gun of the kind studied shows:—
Beam current (μa)   10   50   100   500 1000
Visible spot dia. (in) .047 .056 .06 .068 .083
For the last set of readings, G_1 would be near zero bias.

It is evident we must also look elsewhere than to simple first order electron optics to explain fully these relatively larger spot sizes, and indeed the traces drawn with the final lens models make it clear that spherical aberration is one factor to be examined further.

Spherical aberration

We saw that the path traces through the final lens gave us a qualitative indication of spherical aberration. Recourse is now made to the work of Liebmann[12] (1949), who studied fourteen lenses of the unipotential type. His results enable reasonable assumptions to be made of the abberation coefficients of our lens.

Our lens is something like Liebmann's Nos. 7, 8, 10 and 12—to which the upper line in his Fig. 11 applies. We now calculate a paraxial path through the lens by means of numerical plots using the paraxial equation (see Appendix, Table 2 (b) and (e)), and we find that a path starting off from the cathode at a small angle to the axis meets the axis again when projected at a true distance of 120 in. from the gun (a fact interesting in itself). We thus have a paraxial object distance, i.e. from cathode to centre of lens, viz. 1.1 in; and the image distance 120 in; and taking the thickness of the lens D from Liebmann's work as 0.5 in we find the paraxial focal length f_0 to be 1.115 in, and the parameter $f_0/D = 2.23$. Liebmann's Fig. 11 now gives the aberration parameter $(S - T) = 80$; and by applying his Eq. (9) (loc. cit., p. 216) a number of paths have been calculated and drawn in Fig. 15 for electrons entering the final lens at radial distances of .01 in, .02 in, .03 in, .04 in, .05 in, and .06 in having originated from a point on the axis near the cathode.

Without overestimating the quantitative merit of these path calculations we can say that they give us a good guide to the effect of spherical aberration in the final lens. The contribution of this lens to spot diameter will grow with beam diameter till it amounts to about .03 in when the beam diameter, as it enters the final lens, is .04 in; this contribution then remains stationary till the beam is .08 inches in diameter after which it increases rapidly; so much so that a beam diameter of .12 in appears to correspond to a minimum spot size of nearly 0.3 in.

This diagram therefore clarifies both the growth of spot size with drive and the appearance of spots much greater in size than indicated by a simple first-order theory.

It also throws some light on the formation of "halo" at high beam currents. When a stationary screen spot is observed (under pulsed drive so as not to burn the screen) the spot appears as a very bright kernel surrounded by a halo as the grid is driven to near zero volts. During scanning the halo does not contribute to the bright line, but causes rather a loss of contrast-line to background. When it is recalled that because of the nature of the cathode system the current density is greatest at the centre of the beam, the disposition of paths in Fig. 15 with a concentration in the centre goes a long way towards explaining the structure of the spot at high drive.
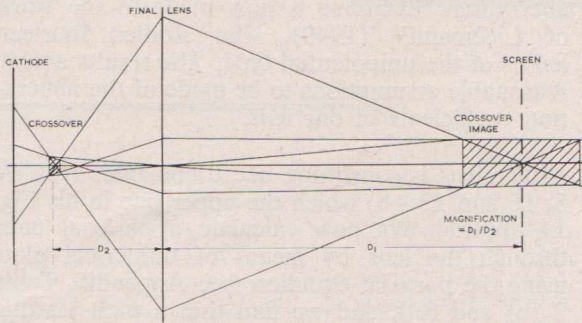
Fig. 14—Paraxial image of crossover, idealised.

This observation is supported by a simple subsidiary experiment in which a large diameter magnetic lens was fitted to a picture tube that did not have a final electrostatic lens (G_4 was connected to G_3 and G_5). This composite gun did not produce "halo"—presumably because spherical aberration due to the large magnetic lens is very much smaller than in the electrostatic lens under study.

Space charge and thermal velocities

We can deduce some limiting figures concerning these two factors by use of the Hollway chart already referred to. We assume a beam current of 1ma and a beam diameter in the gun of 0.1 in. With $V = 16,000$ volts, the chart gives the minimum spot diameter possible with space charge, assuming perfect focussing, as .004 in. Likewise, thermal velocities allow a cathode radius up to twice the spot radius; and hence if the electron optical system were capable of it, we could produce a spot diameter of .01 in,

since at zero bias the diameter of the cathode drawn upon is .02 in.

We thus look to thermal velocity effects to increase the spot size obtainable by no more than .01 in, while space charge effects are not important.

In relation to thermal velocities we of course cannot strictly refer to definite spot sizes as though they corresponded to uniform current density and had sharp edges. The relevant theory usually implies a gaussian distribution across the spot, the spot size quoted being that which would carry the same total current at a constant density across the whole spot. We must assume that the size of the visible spot also involves the variation of current density across the beam due to causes other than random initial velocities. We have little information on all this from the present work, except that we can infer that more current is drawn from the centre of the cathode and that at least early in its path the centre of the beam is the most dense. Spherical aberration produces some mixing of inner and outer paths as the beam nears the screen; and all in all, the distribution of density over the spot appears to be difficult to analyse; and for the sake of simplicity, these effects are ignored.

Again as was shown very clearly by Moss[13], initial transverse velocities much greater than thermal velocities can be introduced by imperfections in an oxide cathode surface, particularly

13. Moss, Hillary, "A note on anomalous radial velocity spectra from rough thermionic emitters", *Journal of Electronics and Control*, **11**, No. 4, October 1961, 289.
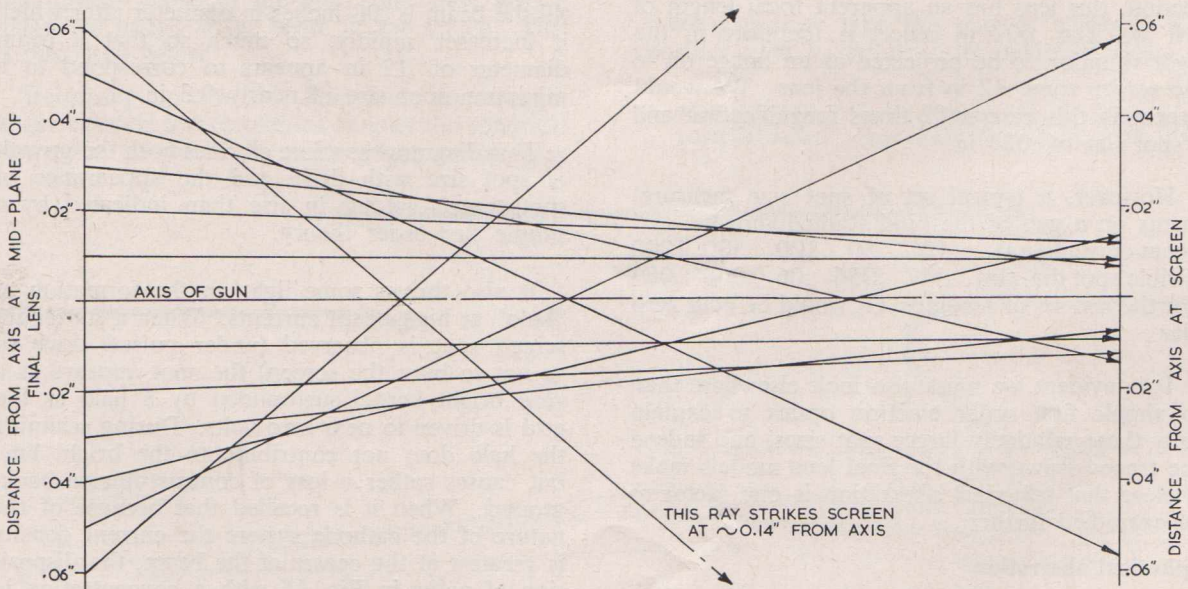

Fig. 15—Aberration of final lens (factor S-T = 80).

when emission is affected. The present discussion applies to smooth, well activated cathodes.

Main factors controlling spot size

We therefore conclude that the principal factors determining spot size are (a) the size of the cross-over and its magnification by the focussing lens system, (b) spherical aberration in the final lens, which becomes important because of the width of the beam as it passes through the final lens and (c) initial velocities generated at the cathode.

There would seem to be some advantages (if finely focussed lines are sought) in keeping the beam as narrow as possible at all points, as this would reduce the effects of (a) and (b). There are however limitations imposed by space-charge spreading. This is well illustrated by an example worked out with the aid of the Hollway chart. We will assume that we can so work out the lens systems that we restrict the maximum diameter of a 1 ma beam to .03 in. From the chart we find the minimum spot imposed by space charge to be .06 in diameter—a very different result from the case considered earlier. A design compromise is necessary if a narrower beam is to be used (see e.g. Franken et. al., loc. cit. These authors also discuss deflection defocussing, which is reduced by a narrower beam.)

It is appropriate at this point to discuss briefly the effects of the G_2 and Ultor voltages on spot size.

Effect of G_2 voltage

Measurements on the 8235 gun do not show up a marked variation in spot size with G_2 voltage—there is perhaps a tendency for the spot to grow with G_2 voltage, which is rather contrary to experience with some designs. There are compensating factors at play; although for a given beam current the effective cathode area will be smaller to compensate the increased potential gradient near the cathode, on the other hand the "necking in" at the cross-over is a little sharper as the cross-over shifts slightly towards the cathode; and the result is a very small change of beam diameter and spot size.

It will of course be appreciated that a higher G_2 voltage will increase the peak cathode current density.

Effect of "Ultor" ($G_3 + G_5$) voltage

It is well known that apparent spot size decreases with increasing Ultor voltage. This is due principally to a number of factors. (a) Phosphor efficiency increases with beam voltage and thus requires a smaller beam current for a given light output. As we have seen beam current and spot size are directly related. Hence for a given level of brightness we have finer lines at the higher Ultor voltages, or in other words an apparently smaller spot size. (b) Initial thermal velocities and space charge are less effective in spreading the spot.

Spot size and line width

A reminder can be given here that a rapidly scanned line of the raster appears much thinner than would be expected from the size of the generating spot. This is well explained in the text books (e.g. see Maloff and Epstein loc. cit., p. 180). In a typical recent measurement, at a beam current of 100 μa, a .065 in diameter spot gave an apparent line width of .04 in.

The Cathode-test Condition

As was stated above, under this condition the final lens is stronger, and forms a cross-over between the gun and the screen, but close to G_5 so that a large spot is produced on the screen. Path D in Fig. 13 represents a typical path as though coming from the cathode, and when extended would cut the axis 1.25 inches from the centre of G_4 (scale of actual gun). Since the screen is about 11 in from this point, and assuming path D to be on the edge of a beam, i.e. the beam is about .1 in in diameter we would have a spot of about 0.8 in formed on the screen.

We return now to Figs. 6 and 9 to trace the passage of the beam through the whole gun under cathode test conditions. Taking the zero bias case, we see that the beam is leaving the G_2 with a spread of 20°, continuing with a numerical trace through the G_2-G_3 lens (see Appendix, Table 2 (c)) we find the outer path forming the edge of the beam leaving the first G_3 aperture at an angle of 3.4° and distant .0215 in from the axis. After a further .6 in travel to the second G_3 aperture, it is distant .058 in from the axis; that is, the beam is .116 in wide at this point. This is about the same as the diameter of the G_3 aperture, and explains why the shadow of this aperture appears during this test when bias approaching zero is used. Path E is sketched in Fig. 13 to correspond to the beam edge at near zero bias. We can judge that it crosses the axis somewhere near path A—say 0.7 in from the centre of the lens. We thus would expect the shadow of the G_3 aperture to have a diameter on the screen of

$$(10.3/.7) \times .120 = 1.75 \text{ in.}$$

which is approximately the figure obtained in practice.

As a further illustration we take a path setting out from the cross-over at a small angle to the axis: 3° is chosen. From Fig. 9 we see that this would correspond to the edge of a beam which starts from a cathode spot .002 in in radius.
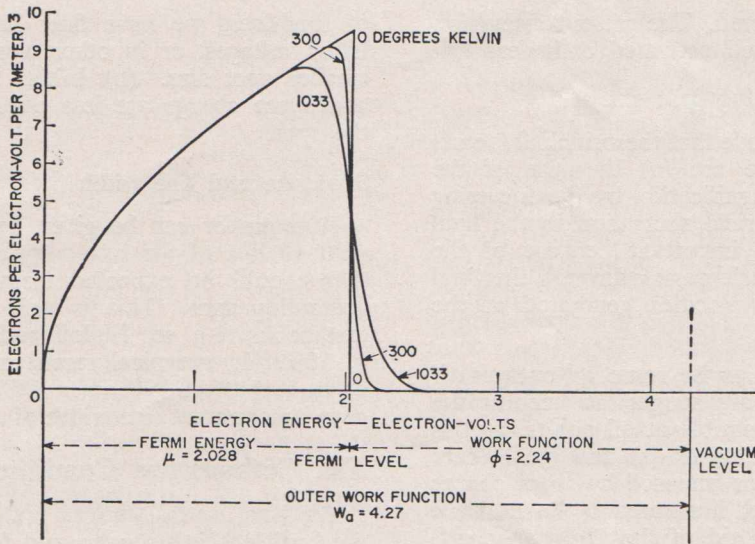
Fig. 2—Energy distribution of conduction electrons in potassium at temperatures of 0, 300 and 1033 degrees Kelvin based on elementary Sommerfeld theory. (ref. 17).

the maximum kinetic energy E of an emitted photoelectron:

$$E = \frac{mv^2}{2} = h\upsilon - \phi \qquad (1)$$

Eq. (1) shows that the maximum energy of the emitted photoelectron $mv^2/2$ is proportional to the energy of the light quanta $h\upsilon$ less the energy ø (the **work function)** which must be given to an electron to allow it to escape the surface of the photocathode. For each metal, the photoelectric effect is characterized by a value of ø, which is usually expressed in electron-volts.

In the energy diagram for a metal shown in Fig. 1, the work function represents the energy which must be given to an electron at the top of the energy distribution to raise it to the level of the potential barrier at the metal-vacuum interface.

According to the quantum theory, only one electron can occupy a particular quantum state of an atom. In a single atom, these states are separated in distinct "shells"; normally only the lower energy states are filled. In an agglomeration of atoms, these states are modified by interaction with neighbouring atoms, particularly for the outermost electrons of the atom. As a result, the outer energy levels tend to overlap and produce a continuous band of possible energy levels, as shown in Fig. 1.

The diagram shown in Fig. 1 is for a temperature of absolute zero; all lower energy levels are filled. As the temperature is increased, some of the electrons absorb thermal energy which permits them to occupy scattered states above the maximum level for absolute zero. The energy distribution of electrons in a particular metal is

shown in Fig. 2 for several different temperatures. At absolute zero, all the lower states are occupied up to the Fermi level. At higher temperatures, there is some excitation to upper levels. The electron density at a particular temperature is described by the Fermi-Dirac energy-distribution function, which indicates the probability of occupation for a quantum state having energy E:

$$f = \frac{1}{1 + \exp.\ [(E - E_f)/kT]} \qquad (2)$$

When E is equal to E_f, the value of f is $\frac{1}{2}$. It is customary to refer to the energy of level E_f, for which there is a 50-per-cent probability of occupancy, as the **Fermi level.** At absolute zero, the Fermi level corresponds to the top of the filled energy distribution. Although the Fermi level is nearly the same at higher temperatures, as at absolute zero, as shown in Fig. 2, it is actually slightly lower. This reduction of the Fermi level occurs because the number of possible energy states increases in a conductor as the square root of E, whereas the probability of occupancy function is symmetrical around a value of $E = E_f$.

If the energy derived from the radiant energy is just sufficient to eject an electron at the Fermi level, the following relation exists:

$$h\upsilon_0 = \phi \qquad (3)$$

υ_0 the threshold frequency of the exciting radiation, is related to the long-wavelength limit λ_0 and the velocity of light c as follows:

$$\lambda_0 = c/\upsilon_0 \qquad (4)$$

The relation may be rewritten to relate the long-wavelength limit to the work function, as follows:

$$\lambda_0 = \frac{12395}{\phi} \text{ angstroms} \qquad (5)$$

Because some of the electrons occupy states slightly higher than the Fermi level, as shown in Fig. 2, excitation of these electrons produces an extended response at the red threshold of the spectral-response characteristic. As a result, there is no abrupt red threshold at normal temperatures, and the true work function cannot be obtained in a simple manner from the spectral-response measurement. However, a universal function devised by Fowler can be used to predict the shape of the spectral-response curve near the threshold; the work function can then be calculated from these data.

Although many attempts have been made to calculate entire spectral-response characteristics for metals, only order-of-magnitude agreement with experiment has been obtained. It was formerly assumed that surface electrons existing in an image-type force field accounted for the threshold emission spectrum. Early work by Tamm and Schubin[1] postulated that a threshold for a "volume photoeffect" occurs at about twice the frequency of that for the surface threshold. More recent work by Mayer and his associates[2] indicates that in fact the threshold for the volume effect and surface effect may be the same. Because electrons in the volume of the metal have been described as "free", there has been a dilemma in the explanation of conservation of momentum in the absorption of photons. This dilemma has been resolved by taking into account the interaction of the free electrons with the periodic field of the crystal lattice of the metal.
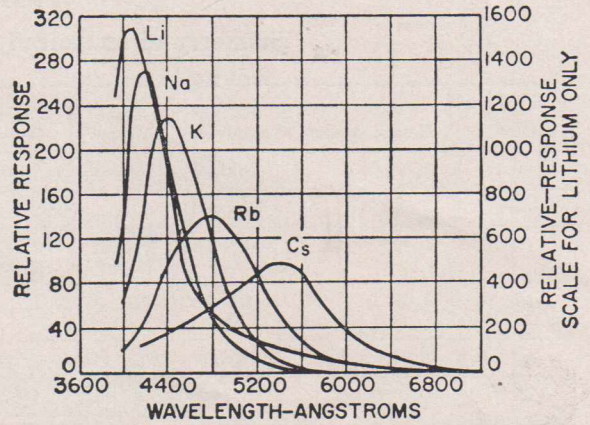

Fig. 3—Spectral-response characteristics for the alkali metals showing regular progression in the order of the periodic table. (ref. 17).

The yield of photoelectrons per incident photon must be low because metals contain large numbers of these free electrons. On the one hand, these electrons result in high optical reflectivity in the visible and near-ultraviolet regions. On the other hand, the free electrons scatter the excited electrons within the metal, reducing the energy available for escape. Consequently, excited electrons originating at a depth of more than 10 angstroms have only a slight chance of escaping. These predictions have been confirmed by measurements of the photoelectric yield in metals, which indicate a **quantum efficiency** of less than 10^{-3} electron per incident photon.

Measurement of the work function and spectral response for clean metal surfaces has been of considerable importance in the development of photoelectric theory. Table I shows a number

TABLE I

Photoelectric work functions and long-wavelength threshold values for pure metals.[17, 18]

Element	Work Function (volts)	Threshold (angstroms)	Element	Work Function (volts)	Threshold (angstroms)
Ag	4.73	2610	Na	2.46	5040*
Al	2.5 — 3.6	3652	Ni	4.86*	2550
Au	4.82	2650	Pb	3.5 — 4.1	2980—3550
Ba	2.51 — 2.52	4920—4940*	Pd	6.30	1962
Bi	4.32*	2870	Pt	6.20*	2000
C	(4.7)	2565—2615	Rb	2.16 — 2.19	5660—5740*
Ca	2.706	4580*	Rh	4.57	2500
Cd	4.24*	2920	Se	5.63* — 4.64*	2200—2670
Ce	2.88*	4300	Sn (B)	4.5	2740
Co	4.25, 4.12	2900, 3000	Sn (Y)	4.38	2820
Cr	4.36*	2840	Sn Liquid	4.21	2925
Cs	1.87 — 1.96	6320—6630*	Sr	2.07*	6000
Cu	4.1 — 4.5	2750—3000	Ta	4.12*	3010
Fe	4.63*	2680	Th	3.40*	3650
Ge	(4.3)	2880	Ti	3.93*	3150
Hg	4.53	2735	U	3.65*	3400
K	2.24	5530*	W	4.59*	2700
Li	2.28	5430*	Zn	3.32	3720
Mg	3.61	3430*	Zn Single Crystals	3.57	3460
Mo	4.35*	2850	Zr	3.76*	3300

* Calculated from $12395/\lambda$ (angstroms) $= \phi$ (volts)

Table 2

Summary of numerically determined paraxial paths

Case	Region of Gun	Voltage Conditions	Trace Starts	Trace Ends	Initial		Final		Path enters final lens at r = (in)
					r (in)	r′	r (in)	r′	
(a)	G_2-G_3	Normal	12% pot'l.	96% pot'l.	.005	.105	.018	.039	.049
(b)	G_2-G_3	Normal	3% ,,	96% ,,	0	.01075	.0009	.0022	.0022
(c)	G_2-G_3	Cathode Test	8% ,,	98% ,,	0	.176	.0217	.059	.058
(d)	G_2-G_3	Cathode Test	8% ,,	98% ,,	0	.0524	.0065	.0175	.017
(e)	Final Lens	Normal	95% at G_3	94.5% at G_5	.0022	.0022	.0032	.000026	—
(f)	Final Lens	Cathode	ditto	ditto	.016	.0165	.013	−.0160	—

The initial conditions in this case are taken from Fig. 9. We note that the path which defines the edge of the beam is .004 in from the axis at the 10% equipotential, and at an angle of 6° to the axis. Thus at our $n = 2$ point, which is about .010 in further along the axis, we have $V_2 = .005$ in, and $V_2' = \tan 6° = .105$ in.

To simplify the arithmetic later we make $\Delta z = 1$, i.e. our unit of length is .04 in.

A small error of no significance is introduced by not carrying the traces right to the 100% potential.

Thus $R_2 = r_2 V^{\frac{1}{4}} = \cdot 125(13)^{\frac{1}{4}} = \cdot 237$

and $R_2' = r_2' V^{\frac{1}{4}} + (r_2/4) V^{-\frac{3}{4}} V' = \cdot 250.$

The numerical work then proceeds as in Table 1.

Finally the values of r_8 and r_8' are calculated from R_8 and R_8' to give $r_8 = .017$ in, $r_8' = .0425 = \tan 2.43°$.

In moving a further .8 in to the centre of the final lens, this path therefore moves out a further .034 in from the axis—a total distance from the axis of .051 in.

The numerical solutions worked out in a number of cases are summarised in Table 2 of this appendix.

Phototubes and Photocells

1: Theory and Measurements

The photosensitive devices described in this article are extremely versatile tools for extending man's sense of sight. The variety of types developed during the past few decades make it possible to equal and surpass many, if not all, of the human eye's remarkable capabilities for detection and observation. These devices exceed the sensitivity of the eye to all the colours of the spectrum, and even penetrate beyond the visible region into the ultraviolet and infrared. They can observe a bullet in flight or track a cosmic-ray particle. They can accompany a rocket into outer space or explore a hole drilled deep into the crust of the earth.

The availability of these devices has led to a wide range of practical applications. **Vacuum-type phototubes** are used primarily for radiation measurement. **Gas-type phototubes** made possible the addition of sound to motion pictures by converting sound patterns traced on film into electrical signals. **Multiplier phototubes,** which have tremendous amplification capability, are used extensively in photoelectric measurement and control devices, and in the large and growing field of scintillation counting. **Photocells** are most widely used in the field of industrial photoelectric control because of their simplicity, low cost, and high sensitivity.

Photoelectric Theory

The earliest observation of a photoelectric effect was made by Becquerel in 1839. He found that when one of a pair of electrodes in an electrolyte was illuminated, a voltage or current resulted. During the latter part of the 19th century, the observation of a photovoltaic effect in selenium led to the development of selenium and cuprous oxide photovoltaic cells.

The emission of electrons resulting from the action of light on a photoemissive surface was a later development. Hertz discovered the photoemission phenomenon in 1887, and in 1888 Hallwachs measured the photocurrent from a zinc plate subjected to ultraviolet radiation. In 1890, Elater and Geitel produced a forerunner of the vacuum phototube which consisted of an evacuated glass bulb containing an alkali metal and an auxiliary electrode used to collect the negative electrical carriers (photoelectrons) emitted by the action of light on the alkali metal.

The development of the transistor and related devices has been closely paralleled by the development of solid-state photosensitive devices, such as photoconductive cells, p-n photojunction cells, phototransistors, and silicon photovoltaic cells used as solar-energy converters.

Photoemission

The modern concept of photo-electricity stems from Einstein's pioneer work for which he received the Nobel Prize. The essence of Einstein's work is the following equation for determining
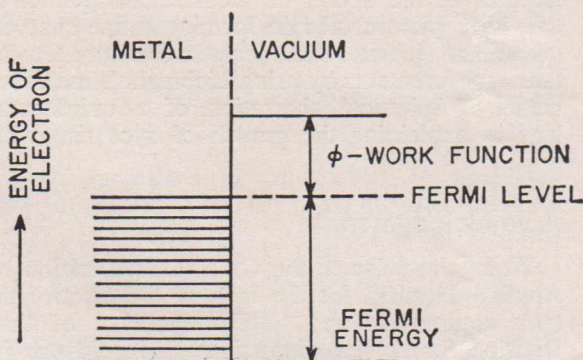

Fig. 1—Energy model for a metal showing the relationship of the work function and the Fermi level.
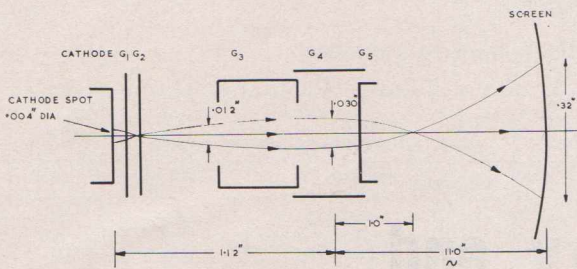
Fig. 16—Beam under cathode test conditions showing magnification of cathode spot.

A numerical trace is now carried out through the whole lens (see Appendix, Table 2 (d) and (f)). This trace shows that this path would pass the first G_3 aperture at .016 in from the axis, and after passing through the final lens will cut the axis a little more than 1 in from the centre of G_4; finally reaching the screen .16 in radially distant from the axis.

The function of the cathode test will now be understood. In its passage from cathode to screen this beam is magnified 80 times (to take the particular case worked out here), and provided there is a reasonable one-to-one correspondence between points on the cathode and points on the screen we have an electron microscope picture (of a sort) of the emission of the cathode, with a magnification great enough to permit the detection of flaws in the cathode surface—caused for example by gas-ion bombardment.

Fig. 16 shows typical electron paths in the gun for the cathode-test conditions. For clarity the scale has been distorted. The dimensions noted apply to the actual case calculated.

In a subsidiary experiment performed by way of further illustrations of this test, a .066 in diameter wire was embedded in the cathode coating of a gun which was then given normal treatment, and finally examined in the picture tube test set under cathode test conditions. A reasonable image of the wire was obtained, the apparent diameter being approximately 0.6 in; i.e. a magnification of 100 was obtained in this case. This is considered as reasonable confirmation of the results worked out from the measurements on the models.

There is no doubt that this test exposes cathode imperfections clearly and its practical value in the factory is immense. It is not easy to understand the clarity of detail which sometimes appears (particularly when the G_3-G_5 voltage is reduced to say 2000 to give greater magnification)—perhaps this clarity of detail is illusory. There will of course be at least a partial formation of a true cathode image in the fashion sketched in Fig. 17 in which we think of principal paths (A, B, C,) each with a bundle of associated paths

formed by initial radial velocities. This sort of image formation will be repeated to some degree in the thick second lens formed by the G_2-G_3 field together with the final lens, and the overall effect could be to reduce the confusion of the final image on the screen. More than this is not to be expected. That there is no real image formation seems to be shown by the fact that alteration of the final lens strength (by G_4 voltage change) simply alters the spot size on the screen without changing its detail at all.

A final point to be mentioned here is that any detail in the spot is only to be seen for low beam currents. The detail remains unchanged for quite a large range of grid bias (e.g. from cut-off at—60 v to—10 v in one case), but then disappears for lower bias values presumably due to confusion introduced by spherical aberration in the wider beam originating from the larger diameter cathode spot.
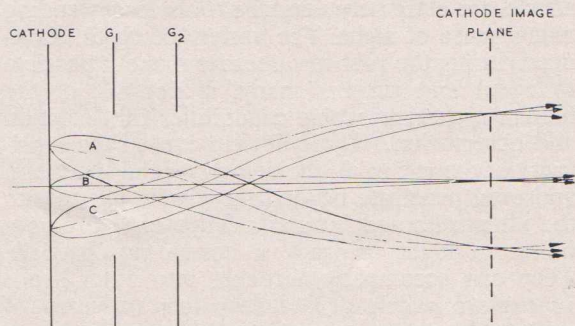

Fig. 17—Idealised picture of formation of cathode image.

Conclusion

It has been shown that the equipment designed by Hollway for drawing equipotential lines and tracing the path of an electron through an electrostatic field, based on the electrolytic tank analogue, can be used to illustrate the main features of the action of the electron gun of a television picture tube in forming a fine spot on the screen. It was found necessary to support the tank measurements by using Liebmann's measurements of spherical aberration of a unipotential lens in explaining the growth of spot size with drive.

Acknowledgments

Table 1

Calculation of path through G_2-G_3 space
Type 8235 gun, normal conditions

n	R_n	R'_n	R_{n+1} (1st val) $= R_n + R'_n$	$\frac{3}{16}\left(\frac{V'_n}{V_n}\right)^2$	$A = \frac{3}{16}\left(\frac{V'_n}{V_n}\right)^2 R_n$	$B = \frac{3}{16}\left(\frac{V'_{n+1}}{V_{n+1}}\right)^2 R_{n+1}$	$C = \frac{A+B}{2}$	$R'_{n+1} = R'_n - C$	$D = \frac{R'_n + R'_{n+1}}{2}$	$R_{n+1} = R_n + D$
1	—	—	—	1.340						
2	.237	.250	.487 .473*	.134	0.318	.0247 .0240	.0283 .0279	.222 .222	.236 .236	.473 .473
3	.473	.222	.695	.0507	.0240	.0231	.0235	.199	.212	.685
4	.685	.199	.884	.0332	.0227	.0276	.0252	.174	.187	.872
5	.872	.174	1.046	.0312	.0272	.0107	.0190	.155	.165	1.037
6	1.037	.155	1.192	.0101	.0105	.0033	.0069	.147	.151	1.184
7	1.184	.147	1.331	.00277	.0034	.0003	.0019	.145	.146	1.330
8	1.330	.145		.00023						

*2nd cycle carried out to demonstrate that a single cycle is sufficient.

based. All the subsidiary experiments reported were carried out by J. Syme (A.W.V.), who also assisted with observations on factory test equipment. F. Stroud (A.W.V.) prepared Fig. 1.

Appendix

Numerical path traces using the paraxial ray equation

The paraxial ray equation is the differential equation for the path of an electron through a symmetrical field, developed by the use of approximations which are valid for paths at all times close to the axis or plane of symmetry[14].

For a cylindrical axially symmetrical electrostatic system, the equation is

$$r'' + \frac{V'r'}{2V} + \frac{V''r}{4V} = 0$$

where V is the potential along the axis,
   r is the distance radially from the axis and the indices ′ and ″ represent the first and second partial derivatives with respect to z, the distance along the axis.

This equation is usually solved by numerical integration and for this purpose is put in the form

$$R'' = -\frac{3}{16}\left(\frac{V'}{V}\right)^2 R$$

by introducing the new variable.

$$R = Vr^{\frac{1}{4}}.$$

In our case we have used the equation to follow paths of very slight curvature, for which the

path tracing equipment is not best suited; and we have also resorted to the method to produce traces when the equipment was not available.

A simple step by step numerical integration is used, in which an extrapolation is followed by a single "iteration" (all that is necessary in our examples). The method is sketched in Pierce[14], p. 103, and it is hoped that the fully quoted example below makes the procedure clear.

Path through G_2-G_3 region, 8235 gun

A graph is drawn from the equipotential plot of Fig. 5, giving potentials along the axis against distance along the axis. A unit of axial length Δz is chosen to give a suitable number of steps— in this case 8 steps are fixed by choosing $\Delta z = .04$ in. At points n = 1, n = 2 . . . etc., at the beginning of each step, V and V′ are determined from the graph, and the following table compiled:—

n	V_n %	V'_n	$\frac{3}{16}\left(\frac{V'_n}{V_n}\right)^2$
1	3.0	8.0	1.34
2	13.0	11.2	.139
3	24.0	12.6	.0516
4	38.0	16.0	.0332
5	56.0	22.8	.0312
6	74.0	17.2	.0101
7	89.0	10.8	.0028
8	96.0	3.4	.00023

14. Pierce, J. R., "Theory and design of electron beams", Chap. 6, Van Nostrand, 1954.
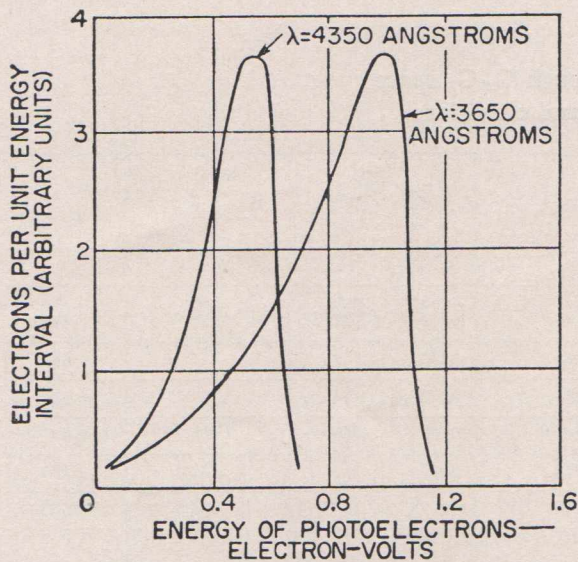
Fig. 4—Energy distribution of photoelectrons from a potassium film. (ref. 4).

of the results obtained. Fig. 3 shows spectral-response curves for the alkali metals.[3] The curves indicate a regular progression of the wavelength for maximum response with atomic number. The most red-sensitive of these metals is cesium, which is widely used in the activation of most commercial phototubes.

The energy distribution of emitted photoelectrons has been measured for a number of metals and photosurfaces. Typical results are shown in Fig. 4 for a potassium film of 20 molecular layers on a base of silver.[4] The maximum emission energy corresponds to that predicted by the Einstein photoelectric equation.

Because a quantum of radiation is necessary to release an electron, the photoelectric current is proportional to the intensity of the radiation. This **first law of photoelectricity** has been verified experimentally over a wide range of light intensities. For most materials, the quantum efficiency is very low; on the best sensitized commercial photosurfaces, the maximum yield reported is as high as one electron for three light quanta.

Research on commercially useful photoemitters has been directed primarily toward developing devices sensitive to visible radiation. The first important commercial photo-surface was silver-oxygen-cesium. This surface, which provides a spectral response designated S-1, is sensitive throughout the entire visible spectrum and into the infrared. Although it has rather low sensitivity and high dark emission, the good response in the red and near-infrared regions provides a spectral response which is a good match to the emission of a tungsten lamp. One of the most important early uses of this photoemitter was in the sound head for motion-picture projectors.

Although other emitters using rubidium and potassium as the principal element were developed, none was of great commercial value until the development of the cesium-antimony photoemitter,[5] which provides an S-4 or S-11 spectral response. The spectral response of the cesium-antimony photocathode includes most of the visible region; maximum response is in the blue and the ultraviolet regions. A recently developed photoemitter,[6] described as multialkali (Sb-K-Na-Cs), provides an S-20 spectral response and is remarkable for its high quantum efficiency and its extended red response.

Because emitters such as the cesium-antimony and the multialkali cathode are semiconductors, the theory developed for metals does not apply in all respects. In a semiconductor, the highest filled energy band for electrons is called the **valence band.** Immediately above the valence band, there is an energy gap for which no electron-energy states exist. This gap is referred to as the **forbidden gap.** In a metal, this gap does not exist and the continuum of energy states directly above the filled energy levels permits conduction. Above the forbidden gap in a semiconductor, there is a band of permitted energy states referred to as the **conduction band,** which at ordinary temperatures contains very few electrons. Fig. 5 shows an energy model for a semiconductor photoemitter. The band-gap energy corresponding to the forbidden gap between the valence and conduction bands is represented by E_g and is expressed in electron-volts. The potential barrier from the bottom of the conduction band to the vacuum outside the semiconductor surface is represented by E_a, the **electron affinity.**
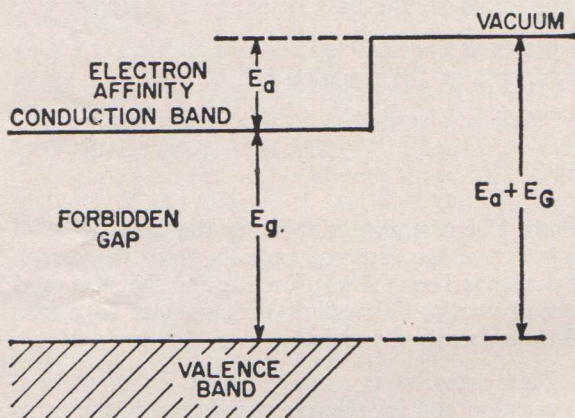

Fig. 5—Energy model of a semiconductor photo-emitter.

When radiation of sufficient energy $h\upsilon$ excites an electron in the valence band causing it to move to the conduction band, photoconductivity may result; however, photoemission does not take place until the electron escapes the barrier to the vacuum. Therefore, the minimum photon energy
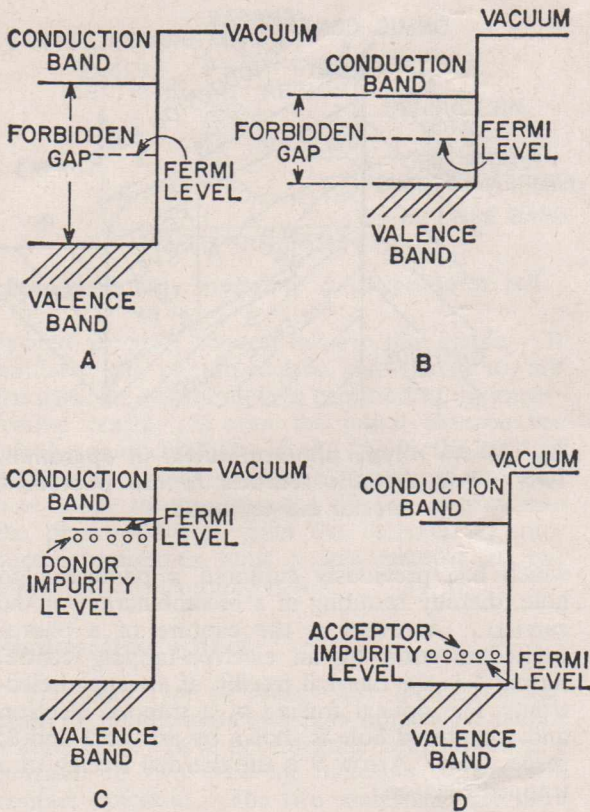
Fig. 6—Energy models for intrinsic and impurity-type semiconductors and for an insulator. (A) an insulator, which has a large forbidden gap. (B) an intrinsic semiconductor, which has a smaller forbidden gap. (C) an n-type impurity semiconductor. (D) a p-type impurity semiconductor.

necessary to produce threshold emission is E_g plus E_a.

For the cesium-antimony photocathode, the value of E_g plus E_a is 2.05 electron-volts; the value of E_a is 0.45 electron-volt. Corresponding values for the multialkali photocathode are 1.55 and 0.55 electron-volts.[7] Although both of these emitters are believed to have impurity (p-type) levels in the band-gap region which account for minor effects, the photoemission is primarily intrinsic (that is, originating from the valence band).

An important advantage of using semiconductors as photoemitters is that their quantum efficiency in the visible spectrum is much higher than that of metals (up to 30 per cent instead of up to 0.1 per cent). In a semiconductor, a photo-excited electron is less likely to lose its energy by electron-electron collision than in a metal. The principal mechanism of energy loss is through the process of impact ionization and pair production, i.e., the creation of a "hole" and electron across the band gap. Usually the threshold energy for such pair production is several times larger than the band-gap energy. In semiconductors in which the electron affinity is small compared with the threshold energy required for pair production, the depth from which an electron can escape may be expected to be large; consequently, the quantum yield should be large, as is actually the case with materials which are practical photoemitters.

Semiconductor Photocells

A photocell is defined as a photosensitive device in which the movement of electrons is in a solid (in contrast to a phototube in which the movement takes place in a vacuum or gas). For photocells, therefore, the electron affinity and emission outside the solid material need not be considered.

The behaviour of semiconductor photocells is most easily explained by reference to energy-state models. Energy models for several types of semiconductors and for an insulator are shown in Fig. 6. The distinction between semiconductor and insulator is arbitrary; materials with band gaps smaller than two electron-volts are usually called semiconductors; those with larger band gaps are called insulators. In an insulator (A), essentially no thermal excitation of electrons from the valence band to the conduction band takes place at normal temperatures. In an intrinsic semiconductor (B), the forbidden gap is sufficiently small to permit some thermal excitation; the amount of excitation increases exponentially with temperature. The thermally excited electrons contribute to a conduction current. The removal of electrons from the filled-band level leaves vacant levels in the energy structure, which are referred to as holes. Electrons of the filled band may then move under the influence of the applied field to fill these holes. As a result, the holes may also contribute to the conductivity as they travel across the semiconductor in the opposite direction from the electrons.

Conduction is also possible in substances which are insulators in the pure state because of the presence of certain impurities or imperfections.
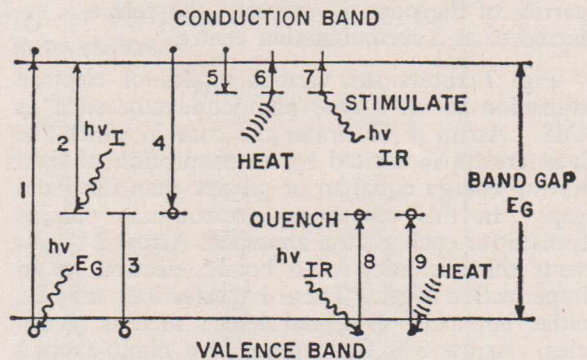

Fig. 7—Basic electronic processes in an n-type photoconductor such as CdS.

Two types of impurity semiconductors are possible; n-type (**donor,** C) and p-type (**acceptor,** D). For an n-type semiconductor, the highest filled quantum level of the impurity lies just below the conduction band of the original or parent lattice (Fig. 6). Conduction becomes possible when electrons from the donor impurity are thermally or otherwise excited to the conduction band.

In the p-type semiconductor, the unfilled level of the impurity lies just above the filled band of the parent lattice. Excitation of an electron from this filled band to the acceptor impurity is then possible and conduction takes place by means of holes in the valence band.

The Fermi levels of these various types of materials are also indicated in Fig. 6. For the insulators and intrinsic semiconductors, the Fermi level lies approximately halfway between the valence and conduction bands; for an impurity-type semiconductor, the Fermi level usually lies in the forbidden band near the impurity level—close to the conduction band in the case of a donor-type impurity, and close to the valence band in the case of an acceptor-type impurity.

Photoconductivity

In photoconductors, currents flow when light excites electrons from the filled band to the conduction band. Conduction may also be produced by the excitation of electrons from an impurity level to the conduction band in an n-type semiconductor or by the excitation of electrons from the filled band to an acceptor level in a p-type semiconductor (in the latter case conduction is by means of holes).

Although excited electrons or holes may travel freely through the photoconductor to the electrodes, they may also be captured by various types of imperfection centres in the photoconductor[8]. If such a capture site provides only temporary retention of the carrier and there is good probability of thermal re-excitation, it is called a **trapping centre.** However, if the capture results in good probability of recombination with a carrier of the opposite polarity, the centre is referred to as a **recombination centre.**

Fig. 7 shows the various modes of electron transition in an n-type photoconductor such as CdS. Arrow 1 illustrates the case in which the host crystal is excited by an absorption of light having energy equal to or greater than the band gap. In this case, one electron-hole pair is formed for each photon absorbed. Arrow 2 represents the excitation of a bound electron at an imperfection level. These imperfections may be either impurities or crystal defects such as vacancies. Arrow 3 is the capture of a photo-excited hole by an imperfection centre. Arrow 4 is the capture of a photo-excited electron by a centre
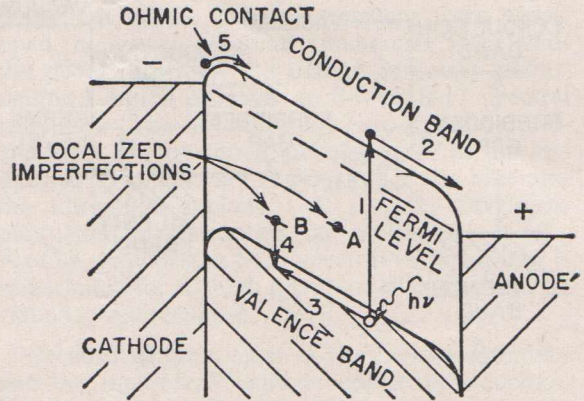

Fig. 8—An n-type photoconductor in operation. Two ohmic metallic contacts to the photoconductor are assumed.

which has previously captured a photo-excited hole, thereby resulting in a recombination of the carriers. Arrow 5 is the capture of a photo-excited electron by an electron-tapping centre. Arrow 6 is the thermal freeing of a trapped electron. The optical freeing of a trapped electron and a captured hole is shown by arrows 7 and 8, respectively. Arrow 9 is the thermal freeing of a trapped electron.

Transitions 1 and 2 determine spectral response; 3 and 4 determine free-electron lifetime and, hence, photoconductivity; 5 and 6 frequently determine speed of response; 7 causes stimulation of conductivity; 8 and 9 correspond to optical and thermal quenching of photoconductivity when the centres involved are those having small cross-section for free electrons. Transitions 3 and 4 may be either radiative, that is, give rise to luminescence emission, or nonradiative.

Because of the relatively low mobility of carriers in semiconductors, space charge usually limits the currents to low values. The effect of the charge is greatly increased by the presence of trapping centres. In some cases, the space-charge fields of trapped holes result in the ejection of electrons from the negative terminal (or those of trapped electrons from the positive terminal) giving rise to a secondary current. As a result of such secondary processes, it is possible to have a quantum efficiency greater than one; that is, one photon results in the movement through the semiconductor of more than one electron. Time delays are observed in the photocurrent which are associated with the time spent by current carriers in traps or recombination centres.[9]

Fig. 8 shows some of these processes for an n-type photoconductor. At condition (1), the absorption of a photon forms a free electron-hole pair; (2) under the applied electric field, the photo-
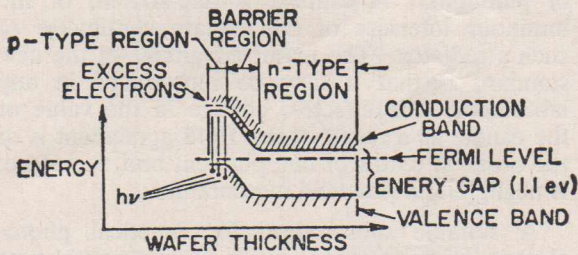
Fig. 9—Energy model of a silicon solar cell.

excited electron moves toward the anode; (3) similarly, the photon-excited hole moves toward the cathode; (4) the hole is captured at an imperfection centre; (5) after the initial electron has left the photoconductor at the anode, the residual positive space charge due to the excess captured hole leads to the entrance of an electron into the photoconductor from the cathode. Photocurrent continues until a free electron recombines with the captured hole.

Photovoltaic Effect

The same type of energy-state model that applies to photoconductors also applies to photovoltaic cells. In a photovoltaic cell, however, a junction of two different materials produces a contact potential. The two materials may be a semiconductor and a metal, or they may be an n- and a p-type semiconductor. The silicon solar cell is this latter type of photovoltaic cell. An n-type silicon wafer is formed with a p-type layer on one surface. The operation of such a cell is illustrated in Fig. 9. The p-type material is shown at the left and the n-type material at the right. For the p-type, the Fermi level lies near the bottom of the forbidden gap; for the n-type, it is near the top. When the two types of silicon are in intimate contact, a potential adjustment takes place across the boundary. Electrons

flow from the n-type material to the lower vacant levels of the p-type material, and holes flow across the boundary in the opposite direction. When the Fermi levels are at the same height, the current ceases to flow, as shown in the potential-energy model. A contact potential equal to the original difference in Fermi levels exists; the p-type material is negative. When the area in the neighborhood of the junction is illuminated, hole-electron pairs are created. The minority carriers created (holes in the n-type silicon and electrons in the p-type silicon) then flow across the junction and constitute the current developed by the photovoltaic cell.

Photoelectric Measurements

Light

Historically, photoelectric measurements and specifications have been related to the measurement of illumination. It is appropriate, therefore, to consider the characteristics of the eye and related photometric units. Although characteristics of the human eye vary from person to person, **standard luminosity coefficients** for the eye were defined by the Commission Internationale de Eclairage (International Commission on Illumination) in 1931. These standard C.I.E. luminosity coefficients are listed in Table II. They represent the relative luminous equivalents of an equal-energy spectrum for each wavelength in the visible range, assuming foveal vision. An absolute "sensitivity" figure established for the standard eye relates photometric units and radiant power units. At 5550 angstroms, the wavelength of maximum sensitivity of the eye, one watt of radiant power corresponds to 680 lumens.

The sensitivity of the eye outside the wavelength limits shown in Table II is very low, but not actually zero. Studies with intense infrared sources have shown that the eye is sensitive to

TABLE II

Standard (C.I.E.) spectral luminous-efficiency values (relative to unity at 555 millimicrons wavelength). These values represent the relative capacity of radiant energy of various wavelengths to produce visual sensations.[12]

Wavelength (angstroms)	C.I.E. Value	Wavelength (angstroms)	C.I.E. Value	Wavelength (angstroms)	C.I.E. Value
3800	0.00004	5100	0.503	6400	0.175
3900	0.00012	5200	0.710	6500	0.107
4000	0.0004	5300	0.862	6600	0.061
4100	0.0012	5400	0.954	6700	0.032
4200	0.0040	5500	0.995	6800	0.017
4300	0.0116	5600	0.995	6900	0.0082
4400	0.023	5700	0.952	7000	0.0041
4500	0.038	5800	0.870	7100	0.0021
4600	0.060	5900	0.757	7200	0.00105
4700	0.091	6000	0.631	7300	0.00052
4800	0.139	6100	0.503	7400	0.00025
4900	0.208	6200	0.381	7500	0.00012
5000	0.323	6300	0.265	7600	0.00006

radiation of wavelength at least as long as 10500 angstroms. Fig. 10 shows a composite curve given by Griffin, Hubbard, and Wald[10] for the sensitivity of the eye for both foveal and peripheral vision from 3600 to 10500 angstroms. According to Goodeve[11] the ultraviolet sensitivity of the eye extends to between 3125 and 3023 angstroms. Below this level, the absorption of radiation by the proteins of the eye lens apparently limits further extension of vision into the ultraviolet. Light having a wavelength of 3023 angstroms is detected by its fluorescent effect in the front part of the eye.

Photometric Units

Photometry deals with the measurement of light in reference to the effect produced on the theoretical standard C.I.E. observer. Measurements are made by visual comparison or by some equivalent photoelectric method. Units, standards, and systems of measurement have been developed to correspond to the effect as observed by the eye.
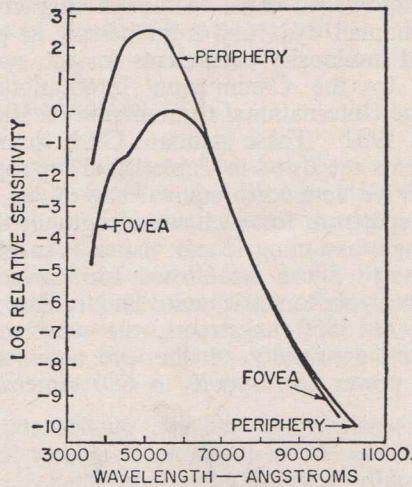

Fig. 10—Relative spectral sensitivity of the dark-adapted fovea and peripheral retina. (ref. 10).

Luminous intensity (or **candle-power**) is a measure of a light source which describes its luminous flux per unit solid angle in a particular direction. For many years the standard measure of luminous intensity was the international candle established by a group of carbon-filament lamps at the Bureau of Standards. In 1948 the International Commission on Illumination agreed on the introduction of a new standard of luminous intensity and recommended the adoption of the name **candela** to distinguish it from the international candle. The term candela is now widely used abroad and is coming into general use in the United States; the older term **candle** is sometimes still used, but refers to the new candle or candela.

The candela is defined by the radiation from a black body at the temperature of solidification of platinum. A candela is one-sixtieth of the luminous intensity of one square centimetre of such a radiator. The major advantage of the new standard is that it may be reproduced in any laboratory. The effective change in the value of the candle as a result of the 1948 agreement is of the order of tenths of one per cent and, therefore, is negligible in practical measurements.

A suitable substandard for practical photoelectric measurements is the developmental-type calibrated lamp, RCA Dev. No. C70048, which operates at a current of about 4.5 amperes and a voltage of 7 to 10 volts. A typical lamp calibrated at a colour temperature of 2870 degrees Kelvin provides a luminous intensity of 55 candelas. The luminous intensity of a tungsten lamp measured in candelas is usually numerically somewhat greater than the power delivered to the lamp in watts.

Luminous flux is the time rate of flow of light energy—that characteristic of radiant energy which produces visual sensation. The unit of luminous flux is the lumen, which is the flux emitted in unit solid angle by a uniform point source of one candela. Such a source produces a total luminous flux of 4π lumens.

A radiant source may be evaluated in terms of luminous flux if the radiant-energy distribution of the sourse is known. If W (λ) is the total radiant power in watts per unit wavelength, total radiant power overall wavelengths is

$$\int_0^\infty W(\lambda)d\lambda,$$

and the total luminous flux L in lumens can be expressed as follows:

$$L = \int_0^\infty [680\,W(\lambda)]\,[y(\lambda)]\,d\lambda \qquad (6)$$

where y (λ) represents the luminosity coefficient (Table II) as a function of wavelength.

The lumen is the most widely used unit in the rating of photoemissive devices. For diode phototubes, typical test levels of luminous flux range from 0.01 to 0.1 lumen; for multiplier phototubes, the range is from 10^{-7} to 10^{-5} lumen (0.1 to 10 microlumens).

Stars of various magnitudes are frequently measured photoelectrically. The flux in lumens L from a star of magnitude m which is received by a telescope having a diameter of d inches can be expressed as follows:

$$2 \cdot 5 \log_{10}(L) = 7 \cdot 57 - 30$$
$$+ 5 \log_{10}(d) - m \qquad (7)$$

An increase of one magnitude indicates a decrease of $\sqrt[5]{100}$ in illumination.
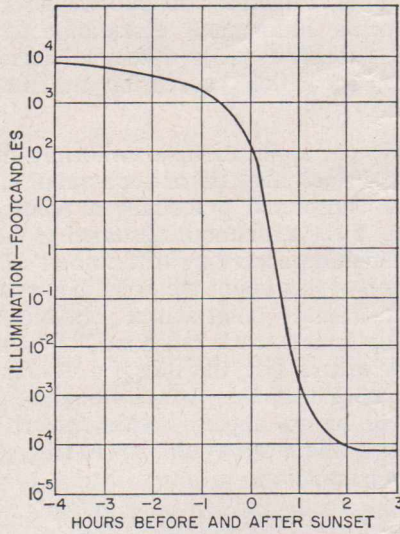
Fig. 11—Natural illumination on the earth for the hours immediately before and after sunset with a clear sky and no moon.

Illumination is the density of luminous flux incident on a surface. A common unit of illumination is the **footcandle,** which is the illumination produced by one lumen uniformly distributed over an area of one square foot. It follows that a source of one candela produces an illumination of one footcandle at a distance of one foot.

Table III lists some common values of illumination encountered in photoelectric applications. Further information concerning natural radiation is shown in Fig. 11, which indicates the change in natural illumination at ground level during, before, and after sunset for a condition of clear sky and no moon.[12]

Photometric luminance (or **brightness**) is a measure of the luminous flux per unit solid angle leaving a surface at a given point in a given direction, per unit of projected area. The term **photometric luminance** is used to distinguish a physically measured luminance from a subjective luminance. The latter varies with illumination because of the shift in spectral response of the eye toward the blue region at lower levels of illumination. The term luminance describes the light emission from a surface, whether the surface is self-luminous or receives its light from some external luminous body.

For a surface which is uniformly diffusing, luminance is the same regardless of the angle from which the surface is viewed. This condition results from the fact that a uniformly diffusing surface obeys Lambert's law, or the cosine law of emission. Thus, both the emission per unit solid angle and the projected area are proportional to the cosine of the angle between the direction of observation and the surface normal.

A logical unit of luminance based on the definition given above is a candela per unit area. When the unit of area is the square metre, this unit is called a **nit;** when the unit of area is a square centimetre, the unit is a **stilb.** It is also possible to refer to a **candela per square foot.** However, none of these units is as commonly used in photoelectric measurement as **footlambert,** which is a unit of photometric luminance equal to $1/\pi$ candela per square foot. The advantage of using the footlambert for a uniform diffuser is that it is equivalent to a total emission of one lumen per square foot from one side of the surface. This relationship can be demonstrated by the following conditions as shown in Fig. 12: an elementary portion of a diffusing surface, having an area of A square feet has a luminance of one footlambert, or $1/\pi$ candela per square foot. Consider the light flux which is emitted into an elementary solid angle, $2\pi \sin \theta \, d\theta$. At an angle of θ, the projection of the elementary area is

TABLE III
Typical values of illumination for various conditions.

Condition	Illumination (Footcandles)
Average solar illumination, 42° N latitude noon, June 21, measured in a plane perpendicular to the sun's rays.	8800
Recommended for reading.	30 to 70
Moonlight.	0.02
Natural night illumination, clear, no moon.*	9×10^{-5}
Natural night illumination, heavily cloudy, no moon.	2×10^{-5}

* Although published data are in some disagreement, it appears that starlight itself is a substantial but not a major component of the quoted figure. Note also that zodiacal radiation in the near-infrared is many orders of magnitude higher than in the visible region.
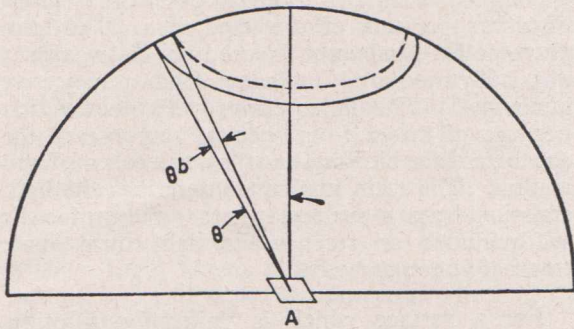
Fig. 12—Diagram illustrating Lambert's law and the calculation of total luminous flux from a diffuse radiation.

equal to A cos θ. Because the luminous flux in a particular direction is equal to the product of the source strength in candelas and the solid angle, the total luminous flux L in lumens from the area may be obtained by integration over the hemisphere as follows:

$$L = \int_0^{\pi/2} \frac{1}{\pi} (A \cos \theta)$$

$$(2\pi \sin \theta) \, d\theta = A \qquad (8)$$

In other words, the total flux from a uniform diffuser having a luminance of one footlambert is one lumen per square foot.

Illumination From Uniformly Diffusing Surfaces

An advantage of the above relationship is that the illumination at a surface in front of and parallel to an extended and uniformly diffusing surface having a luminance of one footlambert is equal to one lumen per square foot or one footcandle. As a result, an instrument reading illumination in footcandles indicates photometric luminance or brightness in footlamberts if the instrument is illuminated essentially from the entire hemisphere. (This statement neglects the possible perturbation caused by the measuring instrument.)

In a typical application, a uniformly diffusing radiating surface may be of such small size that it can be considered practically a point source. However, if the radiator is assumed to be a flat surface radiating according to Lambert's law, the distribution of flux about the point is not the same as for an ordinary point source. In this case, if the surface luminance is one footlambert and the area is A square feet, the flux per steradian in a direction normal to the surface would be A$(1/\pi)$ lumens, or at an angle θ with respect to the normal line the flux would be A$(1/\pi)$ (cos θ) lumens per steradian.

Table IV provides a reference of luminance values for a number of common sources.

All photometric data in this article are presented in units of candelas, lumens, footcandles, and footlamberts; Table V permits conversion to other units if such conversion is required.

Luminous and Absolute Rating Systems

Although the practice of using luminous ratings for photosensitive devices is almost universal in the photoelectric industry, there are situations in which an absolute rating system, or system based on radiant power units instead of photometric units, is more appropriate.

All photodetectors do not have the spectral-sensitivity range of the eye; most do not even closely approximate its spectral response. In the case of an infrared detector, luminous sensitivity is practically meaningless although luminous sensitivity is sometimes arbitrarily defined as the response of the device to the whole radiation of the test source (usually a tungsten lamp) and the

TABLE IV	
Typical values of luminance (photometric brightness) for various sources.[19]	
Source	Luminance (Footlamberts)
Sun, as observed from Earth's surface at meridian.	4.7×10^8
Moon, bright spot, as observed from Earth's surface.	730
Clear blue sky.	2300
Lightning flash.	2×10^{10}
Atomic fission bomb, 0.1 millisecond after firing, 90-feet diameter ball.	6×10^{11}
Tungsten filament lamp, gas-filled, 16 lumen/watt.	2.6×10^6
Plain carbon arc, positive crater.	4.7×10^6
Fluorescent lamp, T-12 bulb, cool white, 430 ma, medium loading.	2000

TABLE V

Conversion table for various photometric units.

1 footcandle (lumen/ft²)	= 10.764	lux (meter candle) (lumen/meter²)
	= 0.001076	phot (lumen/cm²)
1 footlambert (1/π candle/ft²)	= 0.0010764	lambert (1/π candle/cm²)
	= 1.0764	millilamberts
	= 3.426	nits (candle/meter²)
	= 0.0003426	stilbs (candle/cm²)
	= 0.3183	candle/ft²
	= 10.764	apostilbs (1/π candle/meter²)

radiant flux from the lamp is defined by its luminous flux. Sometimes, in order to convey this particular meaning, the term **hololumen** is used in place of lumen. At other times, the device may be rated directly in terms of radiant power—for example, by use of the power in watts projected on the device from a black-body source of prescribed temperature.

In general, the specification of the luminous sensitivity of a device is not sufficiently definitive; the distribution of radiant energy from the source as well as the spectral response of the device and the spectral sensitivity of the eye must be known. However, because many photoelectric devices are fabricated to approximate the visual range, the rating of these devices in luminous terms is convenient, although not entirely unambiguous.

A practical advantage of using luminous standards for testing photoelectric devices is that the test standard usually is a tungsten lamp calibrated for colour temperature and luminous intensity. Secondary standards can readily be prepared by photometric comparison.

Because the spectral emission of the tungsten lamp is known, the radiant sensitivity of a photodevice can be calculated by rather simple procedures if the relative spectral-response charac-

teristic of the device is known.[13] Therefore, the luminous rating is not just an isolated value.

For devices sensitive primarily in the ultraviolet region, the tungsten lamp is a poor standard because of the very small amount of ultraviolet radiation it provides. Such devices are sometimes rated in terms of watts of monochromatic power. Similarly, in the infrared region luminous reference is of doubtful meaning. For this reason, and because infrared-sensitive devices are frequently used as detectors of thermal radiation, such devices are often rated in terms of the radiation of a black body at a temperature that can provide a spectrum rich in the energy of the spectral region characteristic of the device.

Radiant Energy

Black-body radiation.[14] As a body is raised in temperature, it first emits radiation primarily in the invisible infrared region; then, as the temperature is increased, the radiation shifts to the shorter wavelength in the visible spectrum. If the radiating body is one which may be described technically as "black", its behaviour may be accurately described by the laws of radiation. Because the black-body radiation is used as a standard for the infrared region and because other sources may be described in terms of the black body, a brief review of black-body radiation laws and standards is given below.

A black body is one which absorbs all incident radiation; none is transmitted and none is reflected. Because, in thermal equilibrium, thermal radiation balances absorption, it follows that a black body is the most efficient thermal radiator possible. A black body radiates more total power and more power at a particular wavelength than any other thermally radiating source at the same temperature. There are two general theoretical laws which describe the radiation from a black body.

The Stefan-Boltzmann law describes the total radiant flux W per unit area from a black body as a function of temperature, as follows:
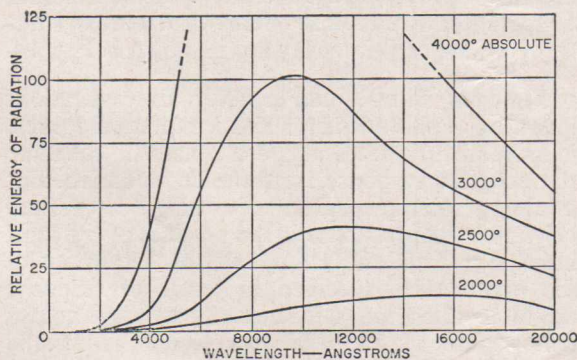
$$W = \sigma T^4 \qquad (9)$$

Fig. 13—Distribution of black-body radiant energy as a function of wavelength at various temperatures.

where σ is equal to 5.6819 x 10⁻¹² watt per square centimetre per degree[4], and T is the temperature of the radiator in degrees Kelvin.

Planck's radiation law describes the spectral distribution of black-body radiation as follows:

$$J\lambda = C_1 \lambda^{-5} (e^{C_2/\lambda T} - 1)^{-1} \qquad (10)$$

where $J\lambda$ is the power in watts in the complete solid angle of 2π steradians on one side of the black-body plane (Lambert's cosine law applying) per unit area for an increment of wavelength of one centimetre; C_1 is equal to 3.7413 x 10⁻¹² square centimetre-watts (the first radiation constant); λ is the wavelength in centemetres; and C_2 is equal to 1.4380 centimetre-degree (the second radiation constant). Fig. 13 illustrates the distribution of black-body radiant energy as a function of wavelength for a number of different temperatures as calculated from Eq. (10).

Although no material is ideally black, the equivalent of a theoretical black body can be achieved in the laboratory by providing a hollow radiator with a small exit hole. The radiation from the hole approaches that from a theoretical black radiator if the area of the cavity is large compared with the area of the exit hole. The characteristic of 100-per-cent absorption is achieved because any radiation entering the hole is reflected many times inside the cavity. For many years experimental physicists had to build their own black-body radiators; however, well-designed commercial radiators are now available.

For a radiation source which is not black, the radiation may be calculated from black-body radiation laws provided the emissivity as a function of wavelength is known. Spectral emissivity $e\lambda$ is defined as the ratio of the output of a radiator at a specific wavelength to that of a black body at the same temperature. Tungsten sources, for which tables of emissivity data are available,[15] are widely used as practical standards, particularly for the visible range. Tungsten radiation standards for the visible range are frequently given in terms of colour temperature, instead of true temperature. The colour temperature of a selective radiator is determined by comparison with the true temperature of a black body; when the output of the selective radiator is the closest possible approximation of a perfect colour match in the range of the visual sensitivity, the colour temperature is numerically the same as the black-body temperature. For a tungsten source, the relative distribution of radiant energy in the visible spectral range is very close to that of a black body although the absolute temperatures differ. However, the match of energy distribution becomes progressively worse in the ultraviolet and infrared spectral regions.

Radiation sources and characteristics. Relative spectral-emission characteristics for a number of important radiation sources are shown in Fig. 14. Each of these sources is described briefly below.

Tungsten lamps are probably the most important type of radiation source for photoelectric applications because of their availability, reliability, and constancy of operating characteristics. Commercial phototube design has been considerably influenced by the characteristics of the tungsten lamp.

The common fluorescent lamp, which is a very efficient light source, consists of an argon-mercury glow discharge in a bulb internally coated with a phosphor that converts ultraviolet radiation from the discharge into useful light output. There are numerous types of fluorescent lamps having different output spectral distribution depending upon the phosphor and gas-filling. The spectral response shown in Fig. 14 is a typical curve for a fluorescent lamp of the "daylight" type.

A very useful point source[16] is the zirconium concentrated-arc lamp. Concentrated-arc lamps are available having ratings from 2 to 300 watts, and in "point" diameters from 0.003 to 0.116 inch. Operation of these lamps requires one special circuit to provide a high starting voltage and another well-filtered and ballasted circuit for operation.

Although many types of electrical discharge have been used as radiation sources, probably the most important are the mercury arc and the carbon arc. The character of the light emitted from the mercury arc varies with pressure and operating conditions. At increasing pressures, the spectral-energy distribution from the arc changes from the typical mercury-line spectra characteristic to an almost continuous spectrum of high intensity in the near-infrared, visible, and ultraviolet regions. Fig. 14 includes the spectral-energy distribution from a water-cooled mercury arc at a pressure of 130 atmospheres. The carbon arc is a source of great intensity and high colour temperature. A typical energy-distribution spectrum of a dc high-intensity arc is shown in Fig. 14.

Matching sources and receiver. In applications involving a photodetector and a radiation source, it is frequently necessary to estimate or calculate the expected response from the combination. For a tungsten-lamp source operating at normal brightness, the response is the product of the luminous flux from the lamp and the sensitivity of the photodevice specified in terms of response per lumen for a tungsten source (a standard colour temperature of 2870 degrees Kelvin is usually specified). For other combinations of source (or source temperature) and receiver, the same simplification does not follow, unless the spectral distribution of the source in the range of the

receiver corresponds closely to that of the tungsten lamp with which the receiver has been calibrated.

In general, the calculation of the expected response of a particular photodetector and a radiation source involves a consideration of the point-by-point match of the spectral emission and the spectral response. Specifically, the response may be calculated as follows:

If $W(\lambda)$ is the radiant power from the source in watts per unit wavelength, the total power from the source is given by

$$W_{Total} = \int_0^\infty W(\lambda) \, d\lambda \qquad (11)$$

If the total power of the source is known (as it usually is) and the relative distribution of the radiant flux is known from data such as Fig. 14, an absolute value of $W(\lambda)$ may be obtained by performing the integration indicated in Eq. (11) with the known relative values $W_{rel}(\lambda)$ and solving for the calibration constant

$$\frac{W(\lambda)}{W_{rel}(\lambda)}.$$

If the receiver has an acceptance area A normal to the line from the source to the receiver, and the distance from the source to the receiver is d, the total power intercepted by the device (assum-
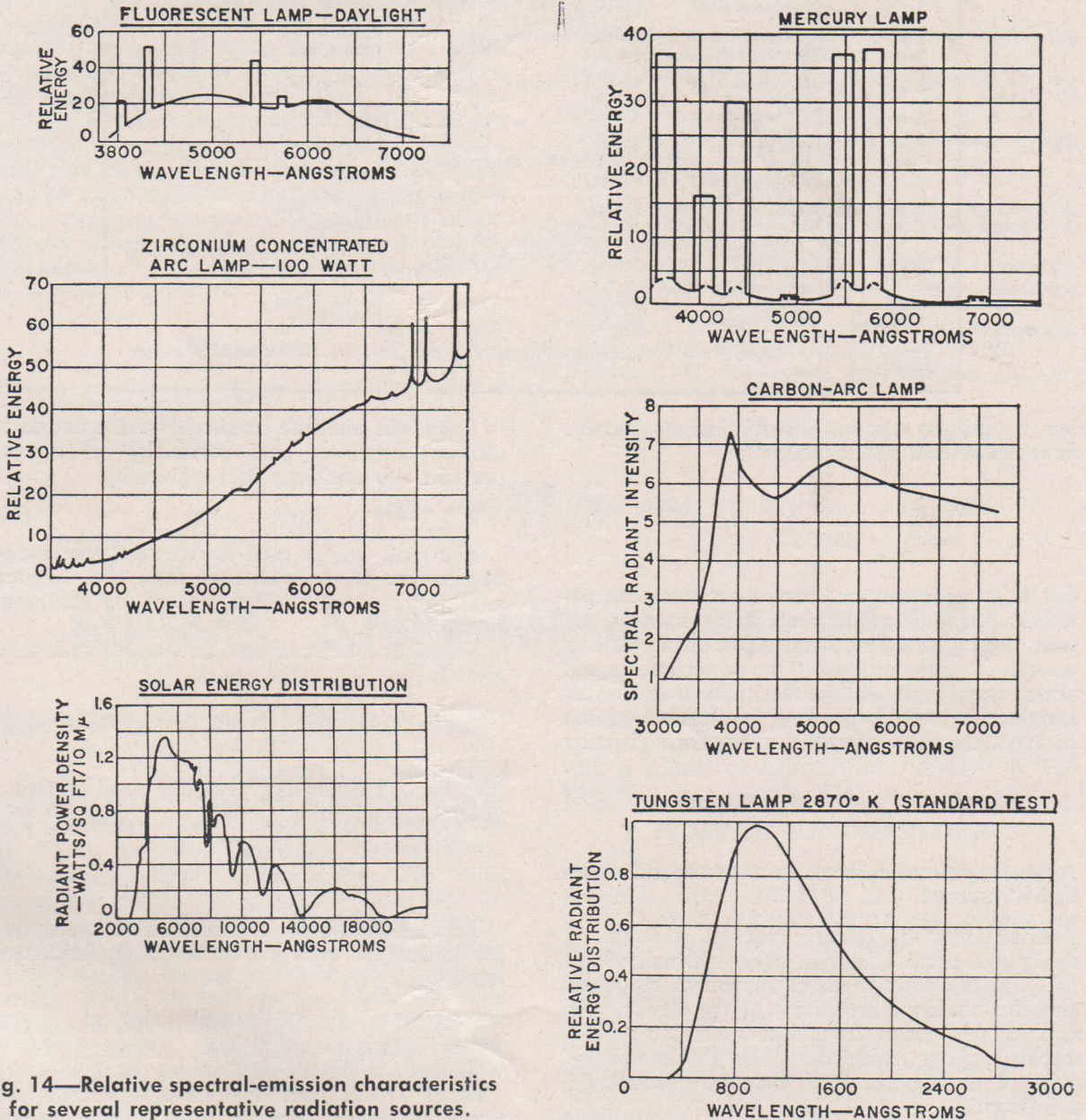
Fig. 14—Relative spectral-emission characteristics for several representative radiation sources.

TABLE VI

Typical combinations of photosensitive surfaces and window materials which can provide the basic spectral-response designations standardized by E.I.A.

Spectral Response Number	Type of Photodetector	Photosensitive Material	Envelope
S-1	Photocathode	Ag-O-Cs	Lime-glass
S-2*			
S-3	Photocathode	Ag-O-Rb	Lime-glass
S-4	Photocathode	Cs-Sb	Lime-glass
S-5	Photocathode	Cs-Sb	UV-transmitting glass
S-6	Photocathode	Na	Unspecified
S-7	Photocathode	Cs-Rb-O-Ag	Pyrex
S-8	Photocathode	Cs-Bi	Lime-glass
S-9	Photocathode	Cs-Sb (semitransparent)	Lime-glass
S-10	Photocathode	Ag-Bi-O-Cs (semitransparent)	Lime-glass
S-11	Photocathode	Cs-Sb (semitransparent)	Lime-glass
S-12	Photoconductor	CdS (crystal with plastic coating)	Lime-glass
S-13	Photocathode	Cs-Sb (semitransparent)	Fused silica
S-14	Photojunction (Photocell)	Ge	Lime-glass
S-15	Photoconductor (Photocell)	CdS (sintered)	Lime-glass
S-16	Photoconductor (Photocell)	CdSe	Lime-glass
S-17	Photocathode	Cs-Sb (reflecting substrate)	Lime-glass
S-18	Photoconductor (Vidicon)	Sb₂S₃	Lime
S-19	Photocathode	Cs-Sb	Fused silica
S-20	Photocathode	Sb-K-Na-Cs (semitransparent)	Lime-glass
S-21	Photocathode	Cs-Sb (semitransparent)	UV-transmitting glass
S-22	Presently unspecified		
S-23	Photocathode	Rb-Te	Fused silica
S-24	Photocathode	Na₂KSb	Lime-glass

* Now obsolete. Formerly a variation similar to S-1, discarded by EIA action to reduce confusion.

ing a uniform spatial distribution of radiant flux) can be expressed as follows:

$$\frac{W_{Total}A}{4\pi d^2} = \frac{A}{4\pi d^2} \int_0^\infty W(\lambda)\, d\lambda \qquad (12)$$

Let $R(\lambda)$ represent the spectral-response characteristic function for the receiver in amperes per watt. Because the response of the device at any wavelength is the product of the power intercepted at that wavelength and the sensitivity at that wavelength, the total response I in amperes of the device to the source for all wavelengths is given by

$$I = \frac{A}{4\pi d^2} \int_0^\infty W(\lambda)\, R(\lambda)\, d\lambda \qquad (13)$$

A linear relationship between response and radiation is assumed.

Given only the relative spectral response of the photosensitive device $r(\lambda)$, normalized to unity at the wavelength of maximum response, and the luminous sensitivity of the device s in amperes per lumen from a tungsten lamp at a specified colour temperature, the absolute sensitivity of the device, $R(\lambda)$, may be calculated[13] as follows:

If σ is the absolute sensitivity of the device at the wavelength of peak sensitivity in amperes per watt, the sensitivity $R(\lambda)$ is given by

$$R(\lambda) = \sigma\, r(\lambda) \qquad (14)$$

The term $w(\lambda)$ is used to represent the energy distribution of the radiation from the tungsten lamp falling on the active area of the photosensitive device.

The light flux in lumens on the device is then given by

$$L = 680 \int_0^\infty y(\lambda)\, w(\lambda)\, d\lambda \qquad (15)$$

(See Eq. 6.) As in Eq. (13), the total current I developed is given by

$$I = \int_0^\infty w(\lambda)\, \sigma\, r(\lambda)\, d\lambda \qquad (16)$$

Because the sensitivity s is specified in amperes per lumen, the equation for s can be written as follows:

$$s = I/L = \frac{\int_0^\infty w(\lambda)\, \sigma\, r(\lambda)\, d\lambda}{680 \int_0^\infty y(\lambda)\, w(\lambda)\, d\lambda} \qquad (17)$$

Finally, the absolute sensitivity of the device in amperes per watt at the wavelength of peak sensitivity can be obtained by solving for σ.

$$\sigma = \frac{680s \int_0^\infty y(\lambda)\, w(\lambda)\, d\lambda}{\int_0^\infty w(\lambda)\, r(\lambda)\, d\lambda} \qquad (18)$$

Because $w(\lambda)$ appears in both the numerator and the denominator, it is not necessary that this value be any more than a relative function showing the distribution of energy from the tungsten lamp.

Spectral-response designation. To facilitate the designation of the spectral response of photodetectors, the manufacturers of such devices through their representation in the Electronic Industries Association (EIA) have set up a series of registered S-numbers which indicate the relative spectral response of the device, i.e., a combination of the transmission characteristic of the envelope or window as well as the basic photosensitivity of the detector element. These numbers are often misused to indicate the photosensitive material or the basic photosensitivity of the detector element alone; it is important to note the distinction. Table VI lists the correct meaning of particular S-numbers.

References

[1] Tamm and Schubin, "Theory of the Photoeffect of Metals", **Z. Physik, 68** (1931).
[2] Mayer, H. and Thomas, H., "External Photoeffect of Alkali Metals", **Z. Physik, 147** (1957).
[3] Seiler, E. F., "Colour Sensitiveness of Photosensitiveness of Photoelectric Cells", **Astrophys. J., 52** (1920).
[4] Brady, J. J., "Energy distribution of Photoelectrons as a Function of the Thickness of a Potassium Film", **Phys. Rev., 46** (1934).
[5] Goerlich, P., **Z. Phys., 101** (1936).
[6] Sommer, A. H., "New Photoemissive Cathodes of High Sensitivity", **Rev. Sci. Instr., 26,** No. 7 (1955).
[7] Spicer, W. E., "Photoemissive, Photoconductive, and Optical Absorption Studies of Alkali-Antimony Compounds", **Phys. Rev., 112,** No. 1 (1958).
[8] Bube, R. H., **Photoconductivity of Solids,** John Wiley & Sons, New York (1960).
[9] Rose, Albert, "An Outline of Some Photoconductive Processes", **RCA Review, 12** (1951).
[10] Griffin, D. R., Hubbard, R. and Wald, G., "The Sensitivity of the Human Eye to Infrared Radiation", **JOSA, 37,** No. 7 (1947).
[11] Goodeve, C. F., "Vision in the Ultraviolet", **Nature** (1934).
[12] **I.E.S. Lighting Handbook,** Illuminating Engineering Society, New York, N.Y. (1959).
[13] Engstrom, R. W., "Absolute Spectral-Response Characteristics of Photosensitive Devices", **RCA Review, 21** (1960).
[14] Forsythe, W. E., **Measurement of Radiant Energy,** McGraw-Hill Book Co., N.Y. (1937).
[15] DeVos, J. C., **Physica, 20** (1954).
[16] Buckingham, W. D. and Deibert, C. R., "Characteristics and Applications of Concentrated-Arc Lamps", **J. Soc. Motion Picture Eng., 47** (1946).
[17] Zworykin, V. K. and Ramberg, E. G., **Photoelectricity and its Application,** John Wiley and Sons, Inc., New York (1949).
[18] Hughes, A. L. and DuBridge, **Photoelectric Phenomena,** McGraw-Hill Book Co., Inc., New York (1932).
[19] Walsh, J. W., **Photometry,** Constable and Co. Ltd., London (1953).

NEWS AND NEW RELEASES

HIGH RESOLUTION PICKUP TUBE

A new 1-inch diameter vidicon TV pickup tube that provides higher resolution than previous high sensitivity vidicons has been developed by the ECD Industrial Tube and Semiconductor Division, Lancaster, Pennsylvania. The tube, designated 8507, is primarily intended for industrial black-and-white TV camera applications, and also promises the possibility of new camera designs for use in commercial broadcast service. It can be used for live black-and-white pickups as well as for film pickups and color TV broadcast service. Resolution capability of the new tube at the centre of the picture is about 1000 TV lines and about 700 lines at the corners. Design of the 8507 includes separate connections for mesh and wall electrodes. This feature makes possible more uniform signal output as well as higher resolution when operated at high voltage.

PLANAR TRANSISTORS

Two new high performance silicon planar transistors—the 2N3119 fast turn-on, high voltage switch and the 2N3118 high voltage vhf amplifier—have been developed by the ECD Industrial Tube and Semiconductor Division, Somerville, N.J. The fast turn-on and high breakdown voltage characteristics of the 2N3119 transistor are ideal for such applications as video amplifier deflection circuits and high voltage core drivers. The 2N3118 has been designed for applications such as an output transistor for small

vhf transmitters, as an injection oscillator or amplifier in vhf receivers, or as a driver for high output vhf transistors such as the 2N2876.

NEW SCR 40216

A new silicon controlled rectifier, 40216, designed for high speed pulse duty at currents to 900 amperes and voltages to 600 volts has been developed by the ECD Industrial Tube and Semi-conductor Division of RCA.

The new device, intended initially for radar pulse modulator applications, can fill a broad range of requirements where extremely fast turn-on of high currents is important. Principal areas of application will probably be in the range of 200 to 900 amperes with a pulse width of 4 to 16 microseconds at repitition rates of 500 to 3500 pulses per second.

The high current performance of the 40216 is a direct result of a unique and coaxial design. The geometry and optimized thermal design of the RCA concentric construction offers a combination of current handling and dissipation capabilities expressed in astronomical numbers. For example, the dI/dt capability of this device is in order of 300×10^6 amperes per second and the switching capability is approximately 500 kilowatts.

QUICK-HEATING POWER VALVE
8462

A new conduction-cooled beam power tube requiring a warm-up time of less than 1 second has been developed by the ECD Industrial Tube and Power Division, Lancaster, Pa. Designed for low voltage mobile or stationary equipment, the 8462 may be used as an rf power-amplifier, oscillator, regulator, distributed amplifier, or linear rf power amplifier.

The fast warm-up of the 8462 eliminates standby filament power in "push to talk" emergency equipment. For extremely rapid warm-up of less than 100 milliseconds, the tube may be used in a suitably designed overvoltage control circuit.